Spin response to localized pumps: Exciton polaritons versus electrons and holes

Vincent Sacksteder, IV,[1,*] A. A. Pervishko,[2] and I. A. Shelykh[2,3,4]
[1]*Division of Physics, Royal Holloway, University of London, Egham, Surrey TW20 0EX, United Kingdom*
[2]*Division of Physics and Applied Physics, Nanyang Technological University 637371, Singapore*
[3]*Science Institute, University of Iceland, Dunhagi-3, IS-107 Reykjavik, Iceland*
[4]*National Research University for Information Technology, Mechanics, and Optics (ITMO), St. Petersburg 197101, Russia*
(Received 31 August 2015; revised manuscript received 7 December 2015; published 18 February 2016)

Polariton polarization can be described in terms of a pseudospin which can be oriented along the x, y, or z axis, similarly to electron and hole spin. Unlike electrons and holes where time-reversal symmetry requires that the spin-orbit interaction be odd in the momentum, the analog of the spin-orbit interaction for polaritons, the so-called TE-TM splitting, is even in the momentum. We calculate and compare spin transport of polariton, electron, and hole systems, in the diffusive regime of many scatterings. After dimensional rescaling diffusive systems with spatially uniform particle densities have identical dynamics, regardless of the particle type. Differences between the three particles appear in spatially nonuniform systems, with pumps at a specific localized point. We consider both oscillating pumps and transient (delta function) pumps. In such systems each particle type produces distinctive spin patterns. The particles can be distinguished by their differing spatial multipole character, their response and resonances in a perpendicular magnetic field, and their relative magnitude which is largest for electrons and weakest for holes. These patterns are manifested both in response to unpolarized pumps which produce in-plane and perpendicular spin signals, and to polarized pumps where the spin precesses from in-plane to out-of-plane and vice versa. These results will be useful for designing systems with large spin polarization signals, for identifying the dominant spin-orbit interaction and measuring subdominant terms in experimental devices, and for measuring the scattering time and the spin-orbit coupling's magnitude.

DOI: 10.1103/PhysRevB.93.085311

I. INTRODUCTION

Quantum particles are characterized not only by their position, but also by additional quantum numbers. Among these quantities the electron's spin, a property which has one of two values, $+1/2$ and $-1/2$, has tremendous promise for improvements in computing technology. If there is no magnetic field which breaks time reversal symmetry, then a 180° rotation reversing an electron's momentum must also reverse the evolution of its spin. Here we will explore diffusive spin transport of an alternate particle, which like electrons has a quantum number with two possible values, but which unlike electrons keeps the same dynamics when momentum is reversed.

The particle of interest is the cavity polariton, the elementary excitation of semiconductor microcavities in the limit of strong coupling between light and the quantum well's excitons. Like electron spin, the polariton has a quantum number with two states: its polarization. Unlike electrons, reversing a polariton's momentum has no effect at all on its polarization. To reverse the polarization's dynamics one must rotate the polariton by 90° not 180°, and thus interchange the x and y axis. (For a review of polarization properties of polaritons see, e.g., Ref. [1].) The consequences of this profound difference for polarization transmission under repeated scattering are at the heart of the current article.

The electron's single-particle density matrix ρ is characterized by charge density N and spin densities S_x, S_y, S_z and can be represented as a vector

$$\rho = [N, \quad S_x, \quad S_y, \quad S_z]. \tag{1}$$

Like the electron, the polariton also has a density matrix composed of its particle density N, circular polarization density S_z, and linear polarization densities S_x, S_y corresponding to xy and diagonal in-plane polarization. In the ballistic regime, i.e., without scattering, the polaritonic analog of spin-orbit coupling causes the polarization's direction to precess, converting linear S_x, S_y polarization to circular S_z polarization and vice versa. For polaritons the axis of precession varies continuously over 360° when the polariton momentum rotates by 180°, unlike electrons where the axis of precession is locked to the momentum. Because of this angular structure, an initial population of linearly polarized S_x or S_y polaritons will evolve into a four-lobed, or quadrupole, pattern of circular S_z polarization. In this celebrated effect, two lobes have positive circular polarization, two have negative polarization, and separating the four lobes is the Langbein cross where the initial linear polarization is unchanged [2–8]. When a perpendicular magnetic field is added, the four-quadrant polarization pattern twists into spiral shapes [8,9].

We will compare the polariton's dynamics under scattering to those of electrons, and also to holes realized in zinc blende semiconductors, where the Fermi level is doped into the $J = 3/2$ valence band rather than the conduction band. In each of these cases we will restrict our analysis to two-dimensional systems analogous to the 2D electron gas. Like polaritons, electrons and holes can be written mathematically as two-state systems, and their dynamics are governed by two-state Hamiltonians. However, unlike polaritons, they possess real spin and therefore must reverse their spin dynamics when their momentum is rotated by 180°. Moreover, in holes (without strain or anisotropy [10,11]) rotating the momentum by 60° also reverses the spin dynamics. This is a consequence of the crystal symmetry, in combination with the fourfold degeneracy

*vincent@sacksteder.com

 ©2016 American Physical Society

of the valence band [12]. Therefore an initial population of S_x holes will evolve into a six-lobed, or sextupole, pattern of S_z spin density. Holes produce six lobes, polaritons produce four lobes, and electrons produce a simple dipole pattern. These qualitative differences in angular dependence correspond to precise differences in the two-state Hamiltonians governing electrons, polaritons, and holes.

In addition to the distinctive spin-orbit splitting terms of each type of particle, we will consider also the effect of a Zeeman splitting term caused by an external magnetic field oriented perpendicularly to the sample. For polaritons this term may also be caused by variations in the polariton cavity such as in-plane strains inside the quantum well, or asymmetries in the direction of crystal growth [1]. This external and tunable parameter is a useful probe of (pseudo)spin dynamics, and in polariton systems is known to twist the polarization pattern into a spiral.

Previous polariton experiments have generally utilized GaAs samples where the clean sample's low disorder density is further diminished by the polariton's large spatial extent, allowing polaritons to move ballistically, i.e., without scattering, on millimeter length scales [13–17]. Ballistic polariton transport has been studied both experimentally and theoretically in many papers [2–9]. It is completely controlled by (pseudo)spin precession: As the polaritons move radially out from the polariton pump, their quadrupole pattern changes sign twice for each precession length l_{prcsn}. The result is that concentric circles of alternating sign are superimposed on the quadrupole pattern [7]. Perfect spin polarization is maintained until the polaritons decay.

In this article we focus on a different scenario, the diffusive regime, where the scattering length is so short that transport is governed by diffusion. We assume that the experimental length and time scales are long compared to the scattering scale. This is the typical case for experiments on 2D electron and hole gases. For polaritons, the diffusive regime can be obtained by fabricating nanopillars embedded in the polariton sample, similarly to optical systems where disorder has been induced by growing nanocolumns [18,19]. In the diffusive case the particle's average displacement r_0 grows according to the diffusive law

$$r_0 = \sqrt{D\,t}, \tag{2}$$

where D is the diffusion constant, unlike the ballistic regime where the rms value of r_0 grows linearly with time. In diffusive samples the momentum becomes randomized through elastic scattering, subject to the constraint that the energy remains equal to the pump energy E_p. Therefore one calculates the average dynamics and transport—averaging over the random disorder, and averaging over the randomized momentum. Performing this averaging, and assuming a low-density, noninteracting system, we calculate the spin diffusion equations which govern the evolution of spin and particle densities. Previous works on polaritons in the diffusive regime used a classical kinetic equation to calculate the equilibrium of steady-state spatially uniform systems [20,21]. Here we calculate the dynamics of nonuniform systems using standard perturbative techniques based in quantum mechanics which have been applied extensively to electron diffusion.

We will show that in the diffusive regime spatially uniform distributions of electrons, polaritons, and holes exhibit identical spin dynamics. The essential reason is that the three particles differ only in their spin-orbit interaction's dependence on momentum, and momentum is randomized by scattering in the diffusive regime. Differences between the spin diffusion equations of the three particles can be resolved only by breaking translational invariance, so we will focus entirely on nonuniform systems.

Previous articles deriving spin diffusion equations have often applied the equations to quasi-1D geometries in steady state, i.e., without temporal dynamics [22,23]. In this case the diffusion equations simplify and can be solved analytically. In this present article we focus instead on the richer and physically relevant case of spatially localized pumps introducing particles into the device at one particular point. Such pumps produce a rich set of interesting spin behaviors. We will show that in the presence of a magnetic field, unpolarized pumps produce through scattering both in-plane and out-of-plane spin densities. Polarized pumps do the same, and in addition exhibit spin precession between in-plane and out-of-plane spins. These signals display spatial multipole patterns with the same angular structure as the spin-orbit coupling—a quadrupole structure in the case of polaritons. If there is a perpendicular magnetic field, the multipoles twist into spirals as time progresses. However, unlike ballistic transport, the spin pattern does not manifest concentric circles around the pump, since transport occurs according to a random walk rather than radial motion.

The structure of this paper is as follows. In Sec. II we explain in detail the electron, polariton, and hole systems which can be realized experimentally, and realistic Hamiltonians for modeling these systems. We also describe how to quantitatively compare diffusive transport of these disparate particles, by rescaling the dimensions and comparing dimensionless ratios. In Sec. III we mathematically prescribe the observables which are calculated in our paper: the density matrix which encodes spin and particle densities, and the response function for a spatially localized pump. Next, Sec. IV presents our analytical results: the diffusion equations which control the evolution of spin densities. These diffusion equations are obtained using a standard technique which has been widely applied to electron diffusion problems [23–30]. Examination of the diffusion equations reveals the multipole pattern which will allow experimentalists to quickly determine the dominant spin-orbit coupling and carefully measure subdominant couplings. Changing the spin-orbit splitting or the scattering time will cause the spatial multipole pattern to rotate. We also show that in a perpendicular magnetic field polaritons and holes exhibit a resonance that can be used to measure the spin-orbit strength. The resonance is characterized by extinction of the polarization produced in response to an unpolarized pump. It occurs at numerically different magnetic field strengths for the two particles, and is sensitive to the spin splitting.

The behavior of a real experimental device cannot be determined unless the diffusion equations of Sec. IV are combined with initial conditions and solved. Unlike previous works which analytically calculated steady-state quasi-1D devices, in Sec. V we solve 2D spin diffusion from a localized pump, using numerical techniques. The problem/solution space is

very rich: oscillating pumps vs. transient pumps, four types of spin input and response (S_x, S_y, S_z, and density N), various angular and radial profiles of the response, time dependence at both short and long times, and an intricate dependence on the relative strengths of the kinetic energy, spin-orbit splitting, Zeeman field, and scattering time. Surveying this complex solution space was one of the chief challenges of the present work. Section V presents the most interesting features. In many cases our results quantitatively confirm and illustrate the qualitative trends discussed in Sec. IV. However Sec. V also gives qualitatively new information: we show that the time evolution breaks naturally into two regimes, before and after loss of memory of the pump polarization. Spin observables can reach quite large values in the first regime, and can persist well beyond the memory loss. We also examine the evolution into spiral structures which will allow measurement of the scattering time, and determine the parameters which maximize the spin polarization. Lastly, Sec. VI synthesizes the major differences between electrons, polaritons, and holes. Several appendices present mathematical details of our calculations.

II. THE MICROSCOPIC HAMILTONIANS FOR ELECTRONS, POLARITONS, AND HOLES

We now introduce a realistic Hamiltonian which models polaritons in a GaAs quantum well, as well as electronic 2DEGs and hole-doped systems [1,12,22]. The spin-orbit coupling varies substantially in these three systems. It is the linear Rashba coupling for electrons, a quadratic coupling for polaritons, and a cubic coupling for holes. We write the Hamiltonian for all three cases in a unified notation with $N = 1$ for electrons, $N = 2$ for polaritons, and $N = 3$ for holes:

$$\begin{aligned} H^N &= \frac{\hbar^2 k^2}{2m} + b_z\sigma_z + \Delta_{SO}\begin{bmatrix} 0 & (k_x - \imath k_y)^N \\ (k_x + \imath k_y)^N & 0 \end{bmatrix} \\ &= \frac{\hbar^2 k^2}{2m} + C\, E_{\text{prcsn}}\sigma_z \\ &\quad + S\, E_{\text{prcsn}} k_F^{-N}\begin{bmatrix} 0 & (k_x - \imath k_y)^N \\ (k_x + \imath k_y)^N & 0 \end{bmatrix}, \\ S &= \sin\theta_B = \frac{\Delta_{SO} k_F^N}{E_{\text{prcsn}}}, \quad C = \cos\theta_B = \frac{b_z}{E_{\text{prcsn}}}, \\ E_{\text{prcsn}} &= \sqrt{\left(\Delta_{SO} k_F^N\right)^2 + b_z^2}, \end{aligned} \tag{3}$$

where $\vec{\sigma} = [\sigma_x, \sigma_y, \sigma_z]$ are the Pauli sigma matrices, $\vec{k}$ is the wave vector, and k_F is the characteristic wave vector determined by the energy E. b_z is the strength of the Zeeman term, and Δ_{SO} controls the strength of the spin-orbit coupling. For convenience we have expressed the relative strength of the Zeeman term and the spin-orbit coupling with the angle $\theta_B = \arctan(\Delta_{SO} k_F^N / b_z)$, a sine $S = \sin\theta_B$, and a cosine $C = \cos\theta_B$. $2E_{\text{prcsn}} = 2\sqrt{(\Delta_{SO} k_F^N)^2 + b_z^2}$ is the splitting between energy levels.

This is a noninteracting Hamiltonian, which works well for polaritons in the limit of low polariton density, where polariton interactions are weak and can be neglected. In this limit the polariton energy E_p—the in-plane kinetic energy in the lower polariton branch—is the same as the energy of the pump photons used to excite the polaritons. Moreover the polaritons' characteristic wave number k_F is the magnitude of $\vec{k}$ on the contour in momentum space defined by $E(\vec{k}) = E_p$. (This contour is the elastic scattering circle for polaritons, or the Fermi surface for electrons and holes.) Note that in the regime of strong pumps nonlinear effects may qualitatively change the texture of the spin patterns [31,32]. The noninteracting picture is also appropriate for electrons in 2DEGs and for hole-doped semiconductors, with the caveat that here E_p is the Fermi energy E_p, and is controlled by doping, gating, etc.

Our $N = 2$ polariton Hamiltonian is accurate when the polariton energy E_p is a fraction of Rabi splitting Ω_R, which is the energy scale of the exciton-photon coupling that produces the polaritons. In GaAs the Rabi splitting is near the value $\Omega_R = 6$ meV seen in Refs. [14–16,33–35], so our Hamiltonian is valid in the range $E_p = [0,2]$ meV. In this article we will fix E_p at 2.0 meV; decreasing this value only rescales the scattering length and time, as well as the polariton wavelength l_p determined by the pump energy. We also choose the mass $m = 5 \times 10^{-5} m_e$, as reported in Refs. [14–16]. This value is typical for polaritons in GaAs quantum wells, and is determined by the band gap in GaAs.

The polarization evolution (or spin evolution for electrons and holes) is determined by the second and third terms in H. The second term is a Zeeman splitting depending on the polarization (or spin) quantum number. Here we assume that this term is oriented along the $\hat{z}$ axis, perpendicularly to the sample, so it produces only in-plane precession.

The third term gives the momentum-dependent spin-orbit coupling, or the TE-TM splitting in the case of the cavity polariton. In polariton systems symmetry arguments require that this term be even in the momentum, which is a very distinctive signature of polaritons. In contrast, in electron and hole systems time-reversal symmetry requires that this term be odd in the momentum, as long as there is no magnetic field or magnetic impurities. The $N = 1$ linear term we use here for electrons is just the Rashba spin-orbit interaction.

The principal source of the quadratic polariton TE-TM splitting is the confined photons' sensitivity to the mirrors of the cavity and to the angle of the incident light [1]. Studies of the TE-TM term and of the Zeeman term (with a modest five Tesla field) have shown that both terms can reach or exceed 0.2 meV, so that they may be comparable to the total polariton energy, and spin-orbit effects can be very large [33,36–40].

A. How to compare electrons, polaritons, and holes

For the purpose of comparison between uncharged polaritons and charged electrons and holes, we neglect the electrical potential Φ and magnetic gauge potential $\vec{A}$ acting on charges. The gauge potential $\vec{A}$ can be neglected if the cyclotron radius is larger than both the scattering length and the dephasing length, which is easily achieved if the sample is not very clean and the temperature is high enough to extinguish weak localization effects. Turning to the electrical potential, a gradient in this potential will cause a net drift of the charges, which will act in addition to the diffusive dynamics considered here. This drift can be be minimized by decreasing the potential gradient.

In the preceding discussion of the Hamiltonian we have taken care to use realistic values for the polariton mass m, pump energy E_p, and spin-orbit coupling strength. However the final results of our calculations are determined only by length and time scales and dimensionless ratios formed from combinations of these parameters. We can compare polariton results directly to electron and hole results by rescaling the dimensions to match each other. Here are the physically relevant scales:

The wavelength l_p and velocity v_p. The mass m and the pump energy E_p (or Fermi energy for electrons and holes) determine the wavelength

$$l_p = h/\sqrt{2mE_p}, \tag{4}$$

which is the fundamental length scale governing transport and dynamics. They also determine the polariton's velocity in ballistic flight,

$$v_p = \sqrt{2E_p/m}, \tag{5}$$

which conveniently allows conversion of times and energies to lengths, and vice versa. At the polariton energy $E_p = 2.0$ meV the polariton wavelength and velocity are respectively $l_p = 4\ \mu$m and $v_p = 4\ \mu$m/ps.

The precession length l_{prcsn}. Taken together, the Zeeman and spin-orbit terms determine the spin (or polarization) precession length

$$l_{\text{prcsn}} = \hbar v_p/E_{\text{prcsn}}, \tag{6}$$

where $E_{\text{prcsn}} = \sqrt{(\Delta_{SO}k_F^N)^2 + b^2}$. We assume that the spin-orbit term is small compared to the kinetic energy $p^2/2m$, or equivalently, that the precession length l_{prcsn} is large compared to $l_p = 4\ \mu$m.

The scattering length l scales with

$$l \propto \frac{(\hbar v_F)^2}{\langle V^2\rangle\, \upsilon^2\, k_F}, \tag{7}$$

where $\langle V^2\rangle$ the second moment of the disorder potential and υ is the characteristic length scale of the impurities. In the diffusive regime only l itself determines the system's evolution, not n or $\langle V^2\rangle$. We do require that the disorder be weak according to the Ioffe-Regel criterion, i.e., that $\chi = l_p/l\pi \ll 1$. Otherwise the diffusion picture breaks down and Anderson-localized states may be observed. To ensure diffusive transport in our polariton system with $l_p = 4\ \mu$m, we set $l = 16\ \mu$m. The scattering time is $\tau = l/v_p = 4$ ps.

The polariton decay length l_{decay}. Unlike electron and hole systems where charge is conserved, polariton number generically decreases with time as photons escape through the Bragg mirrors of the quantum cavity. This decay is determined by the polariton lifetime τ_{decay}, which also determines the maximum distance l_{decay} that polaritons travel before decaying. Under diffusive motion this distance is

$$l_{\text{decay}} = \sqrt{D\tau_{\text{decay}}}, \tag{8}$$

where $D = lv_p/2$ is the 2D diffusion constant. Diffusion can be observed only if the decay length l_{decay} substantially exceeds the scattering length $l = 16\ \mu$m. Therefore we assume a relatively large value $l_{\text{decay}} = 80\ \mu$m, corresponding to $\tau_{\text{decay}} = 200$ ps $= 50\tau$. The (pseudo)spin dynamics of greatest interest occur at shorter time scales of order 10τ, so our numerical results on spin are largely independent of the decay time. For electrons and holes the decay time is infinite.

These numerical values of the polariton decay length and time are experimentally accessible. Polariton cavities far larger than $l_{\text{decay}} = 80\ \mu$m are routinely fabricated in present experiments. Improved mirrors have recently increased the lifetime from a few ps to 180 ps, so 200 ps is also quite feasible [14–16].

Given these length scales, electrons, holes, and polaritons can be compared directly to each other after positions are normalized by the scattering length l and times are normalized by τ. These are the natural length and time scales of a diffusive system. After performing this normalization, only four dimensionless quantities determine the (pseudo)spin dynamics:

(1) The dimensionless disorder strength $\chi = l_p/l\pi = \hbar/E_p\tau \ll 1$.

(2) θ_B, which controls the relative strength of the Zeeman and spin-orbit terms.

(3) The dimensionless diffusion length, $r_0/l = \sqrt{t/2\tau}$, which tracks the diffusive spreading of the initial particles.

(4) The dimensionless energy splitting between the spin up and down states $\zeta = l/l_{\text{prcsn}} = E_{\text{prcsn}}\tau/\hbar$ which determines the dominant source of spin relaxation [41–45].

This last parameter is key to the spin dynamics. $\zeta \gg 1/2$ puts the system in the Elliott-Yafet (EY) regime, where the (pseudo)spin precesses many times before scattering and momentum is tightly coupled to spin. In the EY regime the spin is randomized at every scattering event, so its relaxation time is close to the scattering time τ. In contrast, $\zeta \ll 1/2$ puts the system in the D'yakonov-Perel' (DP) regime where the (pseudo)spin precession length l_{prcsn} is long compared to l, and the energy splitting is small compared to the scattering energy. In this case precession lasts much longer than the scattering time, and the spin relaxation length scales with l_{prcsn}.

As always, we assume that $l_p/l_{\text{prcsn}} = \pi\zeta\chi$ is small, so that the spin splitting is small compared to the kinetic energy $p^2/2m$.

III. THE DENSITY MATRIX AND THE RESPONSE FUNCTION

We now begin developing the equations describing (pseudo)spin dynamics in the diffusive regime, where the particle scatters randomly many times, and where we must average over disorder in order to calculate transport properties. Disorder-averaged diffusive transport is qualitatively different from transport in the ballistic regime, where all transport information is contained in the wave function $|\psi\rangle$. In the diffusive regime scattering randomizes $|\psi\rangle$'s phase and therefore its disorder average $\langle|\psi\rangle\rangle_\epsilon$ averages to zero, losing all transport information. Study of the disorder-averaged wave function alone is unable to describe transport, or even probability conservation, in the diffusive regime.

A correct description of diffusive transport begins with the single-particle density matrix which for the case of a pure state reads

$$\rho(t) = |\psi(t)\rangle \otimes \langle\psi(t)|, \tag{9}$$
$$\rho(t,\vec{x},\vec{\tilde{x}}) = \langle\vec{x}|\psi(t)\rangle\langle\psi(t)|\vec{\tilde{x}}\rangle.$$

The density matrix encodes complete information about the probability density $I(\vec{x})$ in its local $\vec{x} = \vec{x}'$ values:

$$I(t,\vec{x}) = \mathrm{Tr}[\rho(t,\vec{x},\vec{x})]. \tag{10}$$

Here the trace is performed over ρ's spin indices. $I(\vec{x})$ is proportional to the charge density in electron and hole systems, and to the particle density in polariton systems. Similarly, the (pseudo)spin densities are also encoded in ρ's local values:

$$\begin{aligned} S_x(t,\vec{x}) &= \mathrm{Tr}[\rho(t,\vec{x},\vec{x})\,\sigma_x], \\ S_y(t,\vec{x}) &= \mathrm{Tr}[\rho(t,\vec{x},\vec{x})\,\sigma_y], \\ S_z(t,\vec{x}) &= \mathrm{Tr}[\rho(t,\vec{x},\vec{x})\,\sigma_z]. \end{aligned} \tag{11}$$

These local quantities survive the disorder average because of the cancellation of phases between $|\psi\rangle$ and $\langle\psi|$. Nonlocal $\vec{x} \neq \vec{x}'$ values of the density matrix decay exponentially when $\vec{x} - \vec{x}'$ is longer than the scattering length if we are outside the polariton condensation regime [46]. We confine our attention to the local quantities $I(t,\vec{x})$, $S_x(t,\vec{x})$, $S_y(t,\vec{x})$, $S_z(t,\vec{x})$, which are the proper starting point for studying diffusive transport. We write these as a vector:

$$[\rho(t,\vec{x})]^T = \{I(t,\vec{x}),\, S_x(t,\vec{x}),\, S_y(t,\vec{x}),\, S_z(t,\vec{x})\}. \tag{12}$$

It is also convenient to study the spatial Fourier transform of the density matrix, because random disorder after averaging does not break the (average) translational invariance:

$$[\rho(t,\vec{q})]^T = \{I(t,\vec{q}),\, S_x(t,\vec{q}),\, S_y(t,\vec{q}),\, S_z(t,\vec{q})\}. \tag{13}$$

When studying transport with an oscillating pump we will also study the temporal Fourier transform

$$[\rho(\omega,\vec{x})]^T = \int dt\, \exp(\imath\omega t)\, [\rho(t,\vec{x})]^T. \tag{14}$$

It is often useful to compare the spin densities S_i to the probability density I. We define the (pseudo)spin degrees

$$s_x = S_x/I,\; s_y = S_y/I,\; s_z = S_z/I. \tag{15}$$

These degrees can never be larger than 1 or smaller than -1. At one extreme, the density matrix may be entirely unpolarized, in which case it is proportional to $\vec{\rho} = \{1,0,0,0\}$ and the spin degrees are all zero. At the other extreme it may be completely polarized, with $s_x^2 + s_y^2 + s_z^2 = 1$.

A. Response functions

Our goal is to obtain and study a response function $\Phi(t)$ which evolves the density matrix forward in time:

$$\rho(t,\vec{x}) = \int d\vec{x}'\; \Phi(t,\vec{x} - \vec{x}')\, \rho(t=0,\vec{x}'). \tag{16}$$

$\Phi(t,\vec{x},\vec{x}')$ is a 4×4 matrix, because it computes the charge and spin densities at time t as function of the charge and spin densities at $t = 0$. The response function is also a linear operator, which is a direct consequence of our working in the noninteracting regime. Therefore we will study only the response $\Phi(t,\vec{x})$ to a $t = 0$ delta function input $\rho_0\,\delta^2(\vec{x})$ at the origin. The response to any input may be reconstructed from $\Phi(t,\vec{x})$ by convolving the response function over the $t = 0$ density matrix according to Eq. (16).

We will also calculate the temporal Fourier transform $\Phi(\omega,\vec{x})$ which describes the density matrix produced in response to a pump ρ_0 oscillating with period $T = 2\pi/\omega$:

$$\begin{aligned} \Phi(\omega,\vec{x}) &= \int dt\, \exp(\imath\omega t)\, \Phi(t,\vec{x}), \\ \rho(\omega,\vec{x}) &= \int d\vec{x}'\, \Phi(\omega,\vec{x} - \vec{x}')\, \rho_0(\omega,\vec{x}'). \end{aligned} \tag{17}$$

This frequency response function contains both information about the response amplitude and information about the response's phase relative to the pump. Therefore it is in general complex, with both real and imaginary components. In this paper we will study only the magnitude of the response, not its phase information.

Because the system is translationally invariant after averaging over disorder, it is convenient to Fourier-transform both the time response function $\Phi(t,\vec{x})$ and frequency response function $\Phi(\omega,\vec{x})$ to momentum space:

$$\rho(t,\vec{x}) = \int \frac{d\vec{q}}{(2\pi)^D} \exp(\imath\vec{q}\cdot\vec{x})\, \Phi(t,\vec{q})\, \rho(t=0,\vec{q}). \tag{18}$$

We determine the response functions using standard methods from the diagrammatic technique for disordered systems [47]. We neglect effects from quantum interference and adopt a purely classical picture of particle diffusion through the disordered system. We model scattering with a "white noise" disorder potential which does not alter the (pseudo)spin

$$V = \begin{bmatrix} 1 & 0 \\ 0 & 1 \end{bmatrix} u(\vec{r}),\; \langle u(\vec{r})u(\vec{r}')\rangle = (2\pi\nu\tau/\hbar)^{-1}\delta(\vec{r} - \vec{r}'), \tag{19}$$

where the density of states $\nu(E_p)$ at pump energy E_p is

$$\nu(E_p) = \sum_s \int \frac{d\vec{k}}{(2\pi)^D}\, \delta(E_p - E(s,\vec{k})), \tag{20}$$

and $E(s,\vec{k})$ are the two eigenvalues of the Hamiltonian at wave vector $\vec{k}$. We assume that this equilibrium value of ρ is unpolarized, which just means that $E_p > 2E_{\mathrm{prcsn}}$. With this white noise disorder every scattering event causes the particle to lose its memory of its previous momentum, which becomes evenly distributed on the elastic scattering circle. Under these assumptions the time response function can be written as an exponential:

$$\Phi(t,\vec{q}) = \exp\left[\frac{t}{\tau}\, D^{-1}(\vec{q})\right], \quad t > 0. \tag{21}$$

$D^{-1}(\vec{q}) = 1 - I_{ij}$ is the inverse of an operator called the diffuson. It contains information about a single scattering event which is represented by the scattering operator I_{ij}. The response function is obtained by exponentiating D^{-1}, describing the results of repeated scatterings. As a consequence of this exponential form, the frequency response function is

$$\Phi(\omega,\vec{q}) = \frac{1}{\imath\omega + \tau^{-1}D^{-1}(\vec{q})}. \tag{22}$$

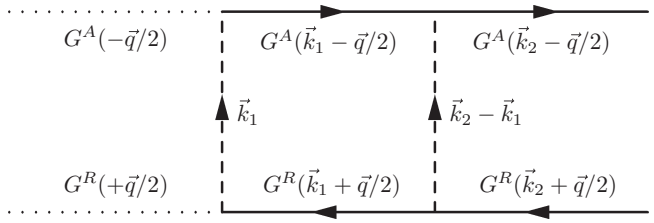

FIG. 1. Diagram illustrating the scattering that produces diffusion. Here two scattering events are shown. G^A and G^R describe time evolution of the polariton ψ and its complex conjugate $\psi^\dagger$. Each scattering event causes correlations between G^A and G^R and is shown as a dashed line connecting the two.

Equivalently to Eqs. (21) and (22), we can also write the spin diffusion equation

$$\frac{\partial}{\partial t}\rho(t,\vec{q}) = D^{-1}(\vec{q})\,\rho(t,\vec{q}). \tag{23}$$

This reveals that D^{-1} is the diffusion operator controlling evolution of the density matrix. Before solving the diffusion equation one must first supplement it with the starting state $\rho(t=0)$.

In the next section we will derive the diffusion operator $D^{-1}(\vec{q})$ analytically. Calculation of the response functions requires numerical calculations—either exponentiation [Eq. (21)] or inversion [Eq. (22)]—and we will perform this numerical work in Sec. V.

IV. ANALYTICAL CALCULATION OF DIFFUSIVE TRANSPORT

In order to calculate the diffusion operator $D^{-1}(\vec{q})$, one must first calculate the scattering operator I_{ij}. In each scattering event the wave function $|\psi\rangle$ and its conjugate $\langle\psi|$ move together, scattering in unison. Two scattering events are pictured in Fig. 1. The scattering operator I_{ij} is given by the integral

$$I_{ij} = \frac{\hbar}{4\pi\nu\tau}\int d\vec{k}\,\mathrm{Tr}[G^A(\vec{k}-\vec{q}/2,E_p)\sigma_i \times G^R(\vec{k}+\vec{q}/2,E_p)\sigma_j]. \tag{24}$$

Here G^A and G^R are the disorder-averaged single-particle Green's functions, and their spectral representation is given in Eq. (C2) in Appendix C. The trace is taken over the spin indices of G^A,G^R,σ_i, and σ_j, which are all 2×2 matrices in (pseudo)spin space. $\vec{q}$ is the diffuson wave vector. Further details of the integration of Eq. (24) are given in Eqs. (C3) and (C4) of Appendix C.

Equation (24) for the scattering operator and $D^{-1}(\vec{q}) = 1 - I_{ij}$ for the diffuson are a well established and widely adopted formalism for determining spin and charge diffusion [23–30]. This formalism has a strong physical motivation expressed in the perturbative diagram in Fig. 1, can be derived from the Keldysh equations for nonequilibrium conduction, and is equivalent to Kubo linear response theory [48]. In the present work we use this formalism to study electrons, polaritons, and holes, in a magnetic field, to all orders of the spin splitting parameter ζ. We also have checked that our results coincide with those of Ref. [22], which is also based on the Keldysh equations, but uses a different strategy for solving them iteratively.

As seen from the Fourier transform in Eq. (18), there is a direct mapping from the momentum $\vec{q}$ to position space. Precisely, every power of $\imath q_x$ corresponds to a ∂/∂_x spatial derivative, every power of $\imath q_y$ corresponds to a ∂/∂_y, and $\imath\vec{q}$ corresponds to $\vec{\nabla}$. Because we are interested only in length scales that are long compared to the scattering length l, we perform a Taylor series expansion of the scattering operator I_{ij} in powers of $l\vec{q}$ (or equivalently in powers of $l\vec{\nabla}$) and terminate the expansion at second order. This approximation is justified for calculating observables at scales larger than l. It guarantees that the inverse diffuson contains only terms with at most two spatial derivatives, which is appropriate for describing particle diffusion under random scattering [22,24]. For the spin-charge coupling in holes we make an exception to this procedure and keep cubic $(lq)^3$ terms, since at quadratic order this coupling is zero, as is well known from previous studies [28,49,50].

As mentioned before, we assume that disorder is weak, far from the localized phase, so that the dimensionless disorder strength $\chi = l_p/\pi l = \hbar/E_p\tau$ is small. Therefore we expand I_{ij} in a Taylor series in powers of χ and truncate at first order. We neglect all powers of χ that do not occur in combination with l, τ, or ζ.

Our spin-orbit term has the special property that the spin splitting $2E_{\mathrm{prcsn}} = 2\sqrt{(\Delta_{SO}k_F^N)^2 + b_z^2}$ is rotationally invariant. As a result we are able to analytically calculate the scattering operator I_{ij} to all orders in the dimensionless energy splitting $\zeta = l/l_{\mathrm{prcsn}}$.

A. The diffuson in the EY and DP regimes

After Taylor-expanding Eq. (24) and integrating over the elastic scattering circle, we find that the inverse diffuson D^{-1} decomposes into four parts: a momentum-independent part λ which gives the spin (or polarization) relaxation rates and the precession term, a diffusion term Δ (not to be confused with the spin-orbit strength Δ_{SO}) which includes the coupling between charge/number density and circular S_z polarization, a momentum-dependent part κ_{0l} which gives the coupling between density and linear S_x,S_y polarization, and a momentum-dependent part κ_{lc} which gives the coupling between linear S_x,S_y polarization and circular S_z polarization. Our decomposition reads

$$D^{-1} = -(\lambda - \Delta + \kappa_{0l} + \kappa_{lc} + \tau/\tau_{\mathrm{decay}}). \tag{25}$$

We present the four terms both in the Elliott-Yafet limit where $\zeta \gg 1/2$, and also in the D'yakonov-Perel' limit where $\zeta \ll 1/2$. In Appendix A we present the more complicated expressions which interpolate between these limits. Appendix C shows gives the details of our derivation of κ_{0l} and also of the coupling between particle density and S_z polarization.

Spatially uniform spin distributions are governed by the mass and precession matrix. Very remarkably, this term is the same for electron, polariton, and hole-doped systems,

regardless of $N = 1,2,3$. It is

$$\lambda^{DP} = \begin{bmatrix} 0 & 0 & 0 & 0 \\ 0 & 2\zeta^2(1+C^2) & 2\zeta C & 0 \\ 0 & -2\zeta C & 2\zeta^2(1+C^2) & 0 \\ 0 & 0 & 0 & 4\zeta^2 S^2 \end{bmatrix},$$

$$\lambda^{EY} = \begin{bmatrix} 0 & 0 & 0 & 0 \\ 0 & (1+C^2)/2 & 0 & 0 \\ 0 & 0 & (1+C^2)/2 & 0 \\ 0 & 0 & 0 & S^2 \end{bmatrix}, \tag{26}$$

where the C and S parameters are defined in Eq. (3). The on-diagonal terms in λ give the (pseudo)spin relaxation rates, which are the inverses of the spin lifetimes. The upper left entry is the inverse lifetime of the charge/number density, and is zero because elastic scattering does not change the polariton number or the electron or hole charge. In the EY $\zeta \gg 1/2$ regime the lifetimes are proportional to the scattering time $\tau = 4$ ps, while in the DP $\zeta \ll 1/2$ regime they scale quadratically with ζ^{-1}; $\tau_{xy}, \tau_z \propto \tau/\zeta^2 \propto \tau^{-1}$.

The off-diagonal terms of λ (zero in the EY regime) describe the usual precession of the in-plane polarization around the magnetic field, which is oriented perpendicularly to the sample, along the z axis. They render the diffuson non-Hermitian, so that its eigenvalues are complex, as required for describing precession. In the DP regime the polarization precesses many—$O(\zeta^{-1})$—times before it decays. In contrast, in the EY regime polarization precession is not visible at diffusive scales, because each scattering randomizes the polarization.

We turn to Δ, the part of the diffuson which is proportional to q^2 and therefore describes diffusion. Since it is zero at zero momentum $q = 0$, it has no effect on spatially uniform distributions.

$$-\Delta^{DP} = \frac{(ql)^2}{2}\begin{bmatrix} 1 & 0 & 0 & d_{0z} \\ 0 & 1 & -6\zeta C & 0 \\ 0 & 6\zeta C & 1 & 0 \\ d_{0z} & 0 & 0 & 1 \end{bmatrix},$$

$$-\Delta^{EY} = \frac{(ql)^2}{2}\begin{bmatrix} 1 & 0 & 0 & d_{0z} \\ 0 & S^2/2 & 0 & 0 \\ 0 & 0 & S^2/2 & 0 \\ d_{0z} & 0 & 0 & C^2 \end{bmatrix},$$

$$d_{0z,N} = -\chi\zeta C + \chi\zeta C S^2 N - \chi\zeta/(1+4\zeta^2)^2\, C S^2 N. \tag{27}$$

The most interesting aspect of this diffusion operator is d_{0z}, the coupling which controls the generation of S_z circular polarization from polariton density (or electron or hole charge). This coupling implies that from an initial population of unpolarized polaritons, diffusive scattering in a magnetic field will produce an S_z signal perpendicular to the plane, with a conversion efficiency controlled by $\chi\zeta = l_p/\pi l_{\mathrm{prcsn}}$. The resulting S_z signal is rotationally symmetric in real space. The d_{0z} coupling describes diffusive generation of S_z polarization inside the structure of the diffuson D^{-1} itself. It is not the same as the external Zeeman potential introduced in Ref. [24], which does not couple S_z to density, and is not part of the diffuson. The d_{0z} coupling requires inclusion of the Zeeman splitting while computing D^{-1}; it is zero when $b_z = 0$, and therefore is omitted in some previous works on diffusion with a Rasha term [22,24].

d_{0z}'s magnitude $\chi\zeta(ql)^2$ is the same for electrons, polaritons, and holes, but its dependence on θ_B, the balance between Zeeman and spin-orbit terms, differs for the three particles. We focus on the EY regime where the last term in d_{0z} can be neglected. In an electron system with linear spin-orbit coupling d_{0z} does not depend on the spin-orbit strength Δ_{SO} at all. Interestingly, in polariton systems if the magnetic field strength $|b_z| = |\Delta_{SO}k_F^2|$ is tuned to exact resonance with the spin-orbit strength, then d_{0z} goes to zero and changes sign. In hole-doped systems with cubic coupling the same resonance is still present, but is shifted to $|b_z| = \sqrt{2}|\Delta_{SO}k_F^3|$. This resonant behavior is interesting both because it is different for electrons, polaritons, and holes, and also because it may be useful for measuring the spin-orbit strength.

The diffusive component Δ contains an additional term Δ^1 which is proportional to $(ql)^{2N}$. Interestingly, it breaks rotational symmetry, mirroring the spin-orbit coupling. In electron systems with a linear Rashba spin-orbit coupling, Δ^1 is

$$\Delta^1 = -e\frac{(ql)^2}{2}\begin{bmatrix} 0 & 0 & 0 & 0 \\ 0 & \cos(2\theta_q) & \sin(2\theta_q) & 0 \\ 0 & \sin(2\theta_q) & -\cos(2\theta_q) & 0 \\ 0 & 0 & 0 & 0 \end{bmatrix},$$

$$e = \frac{2\zeta^2 S^2(3+6\zeta^2+8\zeta^4)}{(1+4\zeta^2)^3}. \tag{28}$$

In the DP $\zeta \ll 1/2$ regime this term is proportional to ζ^2, which is a small contribution to Δ^{DP}. However in the EY $\zeta \gg 1/2$ regime where the spin-orbit coupling is strong Δ^1 is proportional to $S^2/4$, and induces a quadrupole angular dependence in the diffusion. A similar anisotropic diffusion term has been found for spin conduction on the surface of a 3D TI, which because of its strong spin-orbit coupling is in the EY regime [23,51]. More generally, in polaritons Δ^1 scales with $(ql)^4$, and in holes it scales with $(ql)^6$. Because in polaritons and holes Δ^1 is parametrically smaller than the $(ql)^2$ part of Δ, we neglect it in these systems, and retain it only for electrons.

Unlike the treatment of the Rashba coupling in Ref. [22] which leaves the diffusion term constant at its $\zeta = 0$ value where the spin splitting is very small, our result for Δ keeps all orders of ζ. This allows spin or pseudospin to diffuse at a rate different from that of charge or number density, a possibility discussed in Refs. [52–54]. While the diffusion term $\frac{(ql)^2}{2}$ controlling the number/charge density is insensitive to ζ, the other terms in Δ are reduced by the spin-orbit coupling. For instance, the S_z diffusion term (expanded to second order in ζ) is reduced to $\frac{(ql)^2}{2}(1-24\zeta^2)$. This implies that spatial inhomogeneities of number/charge density are smoothed more quickly than spatial inhomogeneities of (pseudo)spin.

We find also a coupling which generates S_x, S_y linear polarization from polariton number density (or electron or hole charge density):

$$\kappa_{0l} = -(\imath q l)^N \gamma_N \begin{bmatrix} 0 & \cos N\theta_q & \sin N\theta_q & 0 \\ \cos N\theta_q & 0 & 0 & 0 \\ \sin N\theta_q & 0 & 0 & 0 \\ 0 & 0 & 0 & 0 \end{bmatrix}, \tag{29}$$

$$\begin{aligned} \gamma_N = {} & \chi\zeta S \times \{(1+C^2)/4, C^2/2, (3/16)(2C^2 - S^2)\} \\ & + \chi\zeta/(1+4\zeta^2)^N \; S(1+C^2) \\ & \times \{-1/4, -1/2, -(9/16)(1-4\zeta^2/3)\}. \end{aligned} \tag{30}$$

This coupling implies that an initial population of unpolarized particles, in the presence of a spin-orbit (TE-TM) splitting, will after diffusion produce a linearly polarized S_x, S_y signal with a conversion efficiency controlled by $\chi\zeta = l_p/\pi l_{\mathrm{prcsn}}$. This process does not occur without a spin-orbit coupling.

Production of linear S_x, S_y polarization from an unpolarized source depends very sensitively on whether the system hosts electrons, polaritons, or holes. First of all, the polarization has a special angular pattern: a dipole pattern in an electron system, a quadrupole pattern in a polariton system, and a sextupole pattern in a hole-doped system. Second, the signal's magnitude is strongly sensitive to the spin-orbit interaction, scaling with ql to the Nth power. At the length scales of interest, much larger than the scattering length l, this implies that the linear polarization is strongest for electrons and weakest for holes. Third, in the DP regime spin production from an unpolarized source is much smaller for electrons than for polaritons or holes. For electrons the two terms in Eq. (30) nearly cancel, giving a signal that scales as $\chi\zeta^3$. In contrast, for polaritons and holes there is no such cancellation and the signal is proportional to $\chi\zeta$, i.e., larger by two factors of the inverse dimensionless spin splitting ζ^{-1}, which is large in the DP regime.

Lastly, the linear polarization's dependence on the Zeeman term is different for each of the three particles. The difference between particles is particularly strong in the EY regime where the second term in γ_N can be neglected, and relatively weak in the DP regime. We focus on the EY regime in the following discussion. In electrons the Zeeman term's influence is weak, changing the polarization by at most a factor of two. In contrast, in polaritons removing the Zeeman term (setting $C = 0$) extinguishes the linear polarization. This means that polaritons, unlike electrons and holes, require a magnetic field to produce a linear spin polarization signal from an unpolarized pump. In holes the requirement is again absent, but one can tune the magnetic field to zero the linear polarization at the resonant condition $|b_z| = |\Delta_{SO}|k_F^3/\sqrt{2}$. As one moves from the EY regime to the DP regime the resonance shifts to smaller $|b_z|$ and eventually disappears. This resonance may be useful for measuring the spin-orbit strength in hole-doped systems.

Finally we turn to the coupling between linear S_x, S_y polarization and circular S_z polarization, κ_{lc}, which describes out-of-plane (pseudo)spin precession. Unlike the couplings d_{0z}, κ_{0l} to the number or charge, the form of κ_{lc} depends strongly on the dimensionless energy splitting ζ, and is independent of the disorder strength χ. It changes if one goes from the DP regime to the EY regime:

$$\kappa_{lc} = -(\imath q l)^N \begin{bmatrix} 0 & 0 & 0 & 0 \\ 0 & 0 & 0 & f_N \cos N\theta_q - g_N \sin N\theta_q \\ 0 & 0 & 0 & f_N \sin N\theta_q + g_N \cos N\theta_q \\ 0 & f_N \cos N\theta_q + g_N \sin N\theta_q & f_N \sin N\theta_q - g_N \cos N\theta_q & 0 \end{bmatrix},$$

$$\begin{aligned} &\text{DP:} \quad f_N = 0,\ g_N = \zeta S \times \{2, -3, 1\}, \\ &\text{EY:} \quad f_N = -CS(-2)^{-N},\ g_N = 0. \end{aligned} \tag{31}$$

This coupling implies that a spin-orbit coupling will cause out-of-plane precession, which converts an initially linearly polarized S_x, S_y signal to circular S_z (pseudo)spin, and vice versa. In the DP regime only a spin-orbit coupling is required, while in the EY regime a magnetic field is also required. In the DP regime this is bona fide spin precession, since the g_N contribution is anti-Hermitian, similarly to the precession term coupling S_x and S_y. In this regime oscillations between S_x, S_y, and S_z are possible. In the EY regime oscillations are not possible because the f_N term is dominant and is Hermitian; we find only a nonoscillatory coupling.

Similarly to κ_{0l} which produces linear polarization from an unpolarized pump, this precession between linear and circular polarization is strongest for electrons and weakest for holes, and the resulting polarization shows a dipole, quadrupole, or sextupole pattern for electrons, polaritons, and holes, respectively. An interesting difference is that the angular pattern rotates by $\pi/(2N)$ during the transition from small ζ to large ζ. This angular pattern is expressed in the coupling's dependence on $\sin N\theta_q$ and $\cos N\theta_q$. These sines and cosines are interchanged when ζ is increased from the DP limit to the EY limit, causing the rotation.

B. Instability and regularization

Our calculation of the response function involved a Taylor series expansion in powers of ql. This is a long-wavelength approximation, restricted to length scales larger than the

scattering length. Outside of this approximation's range of validity, i.e., at momenta $ql > 1$ large enough to probe scales smaller than the scattering length, our analytical formulas predict that the S_x, S_y linear polarization grows exponentially with time instead of decaying, which is an unphysical result. In polariton systems this instability occurs only when $\zeta \propto 1/2$ is near the transition between the EY and DP regimes, i.e., when the spin precession length matches the scattering length.

We have regularized this instability by making an *ad hoc* modification of the diffuson, i.e., a cutoff, when $\frac{1}{2} < (ql)^2$. This cutoff is technically sound and justified because we already removed all short-distance physics when we truncated higher spatial derivatives [22,24]. We have recalculated our numerical results with three different cutoffs, and we compared the results. When the computed results differ, this signifies that they are sensitive to ballistic physics, i.e., length scales smaller than the scattering length l. Throughout our numerical discussion we report which results are stable, independent of the cutoff, and which results do vary with the cutoff because of a sensitivity to ballistic physics. Appendix B describes each of the three cutoffs in more detail.

The numerical results presented in our graphs are calculated with a smooth cutoff that turns on smoothly over the interval $\frac{1}{2} < (ql)^2 < 2$. This cutoff nonetheless produces a spatial oscillation, or ringing, in some of our results. The ringing has a length scale set by the cutoff scale l and affects all components of the density matrix.

C. Summary of analytical results

Remarkably, electron, polariton, and hole systems have identical behavior for spatially uniform spin and charge densities. Their spin relaxation rates and precession are exactly the same. Moreover, there is neither coupling between linear and circular (pseudo)spin, nor between number/charge density and spin.

The behavior of spatially inhomogeneous systems is more intriguing. An initially unpolarized and nonuniform pump will spontaneously produce both circular and linear polarization. The resulting circular polarization has the same magnitude for all three types of particles, but for holes and polaritons in the EY regime it can be zeroed by tuning the magnetic field to a resonance condition where the magnetic field matches the spin-orbit coupling. The resonance condition differs for holes and polaritons. In addition to the circular polarization, the linear polarization also can be zeroed in the EY regime by tuning the magnetic field to a resonance with the spin-orbit coupling, but only in holes.

We have also seen that an initially polarized pump will undergo out-of-plane precession, converting linear polarization to circular polarization and vice versa. Both this process and the production of linear polarization from an unpolarized pump are strongest for electrons and weakest for holes, and produce distinctive dipole, quadrupole, and sextupole patterns for the three types of particles. In the case of out-of-plane precession, this pattern's magnitude and angular orientation are both sensitive to the dimensionless energy splitting ζ.

The analytical results presented here were obtained with a spatial Fourier transform, i.e., in momentum space, and they determine the matrix D^{-1} which controls time evolution. We now turn to numerical calculation of the response function Φ in real space. These numerical results will give us a clear picture of both the spatial distributions that are produced from a spatially localized pump, and of the spin polarization signals that occur before and after the spin relaxation time.

V. NUMERICAL RESULTS

In the previous analytical section we calculated the diffusion operator $D^{-1}(\vec{q})$ in momentum space, which we presented in Eqs. (25)–(31). The response function Φ in momentum space cannot be obtained without numerical calculation, either inverting $\imath\omega + \tau^{-1}D^{-1}$ to obtain the frequency response $\Phi(\omega,\vec{q})$, or exponentiating $\frac{t}{\tau}D^{-1}$ to obtain the time response $\Phi(t,\vec{q})$. Calculation of the real-space response functions $\Phi(t,\vec{x})$, $\Phi(\omega,\vec{x})$ requires a further Fourier transform; we discretize on a spatial lattice and use fast Fourier transforms. The lattice spacing a adds an additional smearing of the response function Φ over an area a^2, in addition to our diffusive approximation which removes ballistic physics at scales smaller than the scattering length l. If $a < l$ this lattice-induced smearing is insignificant. We employ periodic boundary conditions for numerical convenience, combined with large sample sizes. In experimental realizations if polaritons reach the device edges before they decay, then they escape from the edges of the device. The behavior of electrons and holes at device edges is sensitive to attached leads. In the diffusive regime these effects are not significant for the large sample sizes which we employ here.

A. Basic spin precession and decay

We begin our numerical results with two graphs that illustrate quantitatively basic features of the diffusion equations in momentum space. First, Fig. 2 studies the spin precession and decay of systems with fixed wave vector. Figure 2(a) illustrates precession of an initially $\hat{x}$-polarized density which is spatially uniform (zero momentum $\vec{q} = 0$) and therefore shows only in-plane and no out-of-plane precession. The in-plane precession is caused by the Zeeman field oriented perpendicularly to the sample, and is manifested as out-of-phase oscillations of the S_x and S_y linear polarizations (orange and red lines). Dashed lines show precession with only a Zeeman splitting, and solid lines show precession with both a Zeeman splitting and a spin-orbit term. The black solid line shows the overall polariton density, which decays exponentially due to the effects of the finite polariton lifetime. Identical results are obtained for electrons and for holes, which at uniform density have identical spin relaxation dynamics. Of course, because the lifetime of electron and hole charge is infinite, their total density is conserved.

Panel (b) of Fig. 2 shows out-of-plane spin precession, where circular S_z polarization is generated from the initial $\hat{x}$ polarized pump. Unlike panel (a) where we plotted the polarization densities S_x, S_y, here we plot the polarization degrees s_x, s_y, s_z, which are the polarization densities divided by the polariton density I. We will plot this observable s in all subsequent graphs because it shows out-of-plane precession more clearly than the polarization densities S and moreover can be measured easily in experiments. In order to obtain

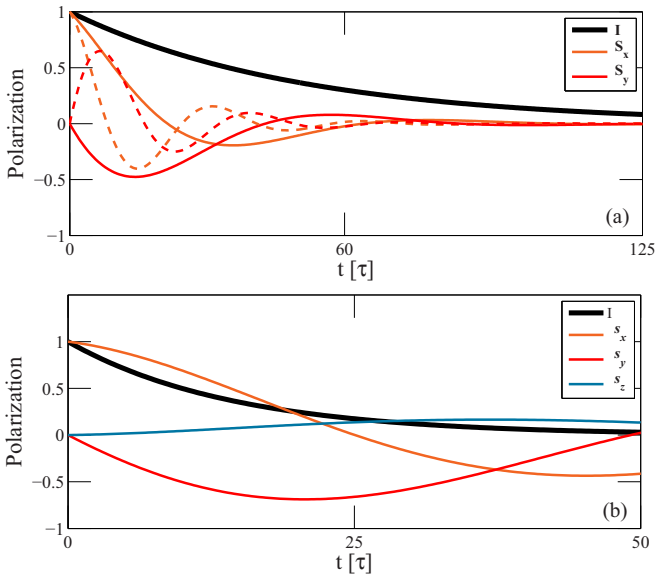

FIG. 2. Polarization precession. The black lines show the polariton density, and the orange, red, and blue lines show linear S_x, S_y and circular S_z polarization. Polarization density S is shown in panel (a), and polarization degree s is shown in panel (b). The initial polaritons are 100% linearly $\hat{x}$ polarized. In panel (a) the initial polariton density is spatially uniform producing strictly in-plane precession, while in panel (b) it has wave vector $ql = 1/\sqrt{10}$ which allows out-of-plane precession. Panel (a) shows in-plane spin precession–out-of-phase oscillations of the S_x, S_y polarizations. Solid lines show precession with both Zeeman and spin-orbit terms ($\theta_B = 5\pi/8$), and dashed lines show precession with only a Zeeman term ($\theta_B = 0$.) Panel (b) shows out-of-plane precession, which produces circular S_z polarization. $\zeta = 0.1, \chi = \hbar/E_p\tau = 1/4\pi$, $\tau_{\text{decay}} = 50\tau$, and $\tau = 4$ ps. In panel (b) $\theta_B = 5\pi/8$.

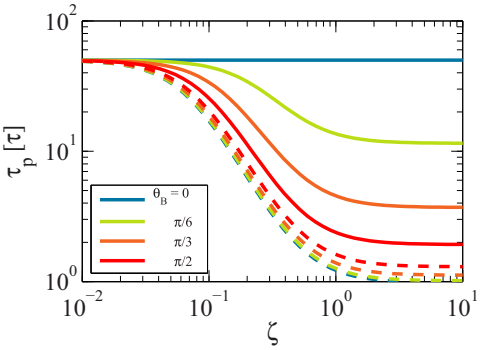

FIG. 3. Polarization (spin) relaxation times τ_p as a function of the dimensionless spin splitting ζ, both for circular S_z polarization (unbroken lines) and for linear S_x polarization (dashed lines.) We plot τ_p at four values of $\theta_B = 0, \pi/6, \pi/3, \pi/2$. In the EY $\zeta \gg 1/2$ regime the decay time is constant, and in the DP $\zeta \ll 1/2$ regime it scales with ζ^{-2}. $\chi = \hbar/E_p\tau = 1/4\pi$, $\tau_{\text{decay}} = 200$ ps $= 50\tau$, and $\tau = 4$ ps.

out-of-plane precession, the polariton distribution must have nonzero wave vector, which we have set to $\vec{q} = \hat{x}/l\sqrt{10}$. The largest polarization degrees are found at large times $t \gg \tau$. At time $t = 50\tau$ the polariton density is about 3.0% of the initial value, the initial 100% $\hat{x}$ polarization degree has reversed sign and is 41%, and a 13% circular polarization degree has been generated.

In Fig. 3 we show the polarization relaxation times of a spatially uniform distribution as a function of ζ. Identical results are obtained for electrons, polaritons, and holes, which in the case of spatially uniform systems have identical spin relaxation dynamics. We show τ_p at four values of θ_B. The D'yakonov-Perel' $\zeta \ll 1/2$ regime is shown on the left side, and the Elliott-Yafet regime $\zeta \gg 1/2$ regime is shown on the right side. In the EY regime τ_p is locked to the scattering time τ, and in the DP regime it scales with ζ^{-2}. At very small ζ the polariton decay time $\tau_{\text{decay}} = 50\tau$ caps τ_p. In electron and hole systems this cap is removed and τ_p continues to scale with ζ^{-2} even at very small ζ.

The straight solid blue line in Fig. 3 shows that when $\theta_B = 0$, i.e., when the spin-orbit coupling is zero, the circular S_z polarization lifetime is equal to the polariton lifetime τ_{decay}. In this case σ_z commutes with the Hamiltonian and circular polarization is conserved. Therefore we find large accumulations of circular S_z polarization when θ_B is small, i.e., when the spin-orbit coupling is small.

B. The polarization's dependence on radius

Next we begin our study of the response to a spatially localized pump, which requires numerical evaluation of Eqs. (21) and (22). In order to learn about typical length scales, Fig. 4 focuses on the radial dependence of the polarization. We present radial data for polaritons only because the electron and hole results are quantitatively similar and qualitatively identical. The similarity of the radial dependence between the three particles, and indeed all of the qualitative and quantitative results seen in Fig. 4 and discussed here, was inaccessible without numerical calculations.

The left panels of Fig. 4 show the temporal response at times $t = 5\tau$, 20τ, 80τ after the pulse, and the right panels show the frequency response to an oscillating signal with periods $T = 5\tau$, 20τ, 80τ. The blue lines in the right panels show the response to a static pump. In the $t, T = 5\tau, 20\tau$ calculations we used a system of size $L = W = 51.2\,l$ and a lattice spacing $a = 0.2\,l$. In the $t, T = 80\tau$ calculations $L = W = 102.4\,l$ and $a = 0.4\,l$, and in the static calculation $L = W = 204.8\,l$ and $a = 0.4\,l$. Since $a \ll l$, lattice-spacing effects are insignificant. We rms-averaged the intensity I and polarizations S_x, S_y, S_z over the polar angle ϕ. The averaged polarization degrees $\langle s_x, s_y, s_z \rangle_\phi$ are calculated by dividing the rms average of S_x, S_y, S_z by the rms average of I.

The upper panels of Fig. 4 plot the polariton density I, which is independent of ζ, and also independent of θ_B and of the starting polarization, except for small variations when $\theta_B = 0$. In panel (a) the time-response curves are simple quadratics, and they match perfectly after rescaling r by $\sqrt{Dt}$, which shows that the polariton density is simply an expanding Gaussian. Similarly in panel (b) the frequency response curves coincide well after rescaling by $r_0 = \sqrt{DT}$. The frequency response decays exponentially with r for all $r/r_0 > 0.3$. (We obtain a good match for the static data by rescaling with the artificial value $T = 1280$ ps. This value of T may be

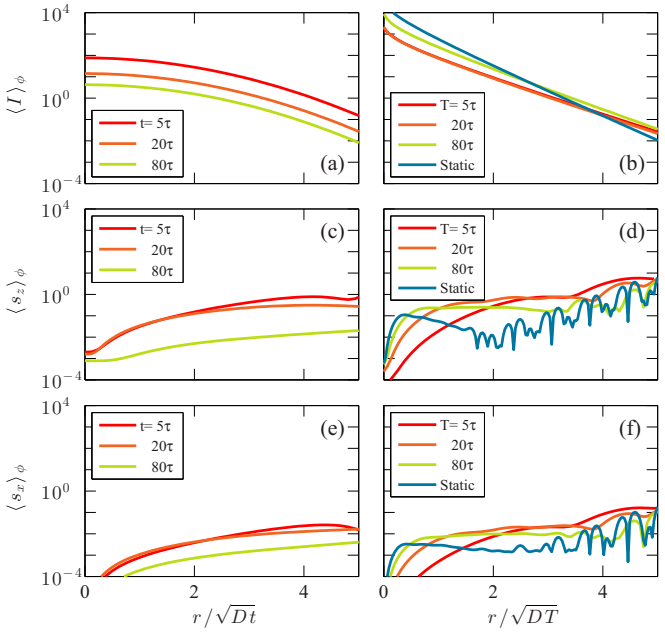

FIG. 4. Radial distribution of the polariton density and polarization degree. The left panels show the time response $\rho(t,\vec{x})$ at time t to a transient pulse, while the right panels show the frequency response to an oscillating signal with period T. All panels show the signal's radial dependence, after performing an rms average over the polar angle ϕ. The radial coordinate is rescaled by the diffusion length $r_0 = \sqrt{Dt}$. The upper panels plot the polariton density $\langle I \rangle_\phi$ (in arbitrary units) produced by an unpolarized pump, the middle panels plot the circular polarization degree $\langle s_z \rangle_\phi$ produced by out-of-plane precession from a linearly polarized pump, and the bottom panels plot the linear polarization degree $\langle s_x \rangle_\phi$ produced by an unpolarized pump. For polaritons $\tau_{\text{decay}} = 50\tau$. $\zeta = 0.1$, $\theta_B = 5\pi/8$, $\chi = \hbar/E_p\tau = 1/4\pi$, $\tau = 4$ ps.

tied to the decay time $\tau_{\text{decay}} = 200$ ps.) The density's almost perfect insensitivity to ζ, θ_B, and time t, T, after rescaling the radius r, supports our use of intensity variables s_x, s_y, s_z in the remaining graphs. Because I has a simple profile, dividing by I does not obscure or complicate the physics revealed in the following graphs.

The density's form is very similar to that of a simple particle density undergoing diffusion without spin-orbit coupling or spin precession. In this case the diffusion operator is just $D\tau q^2$, where D is the diffusion constant, and the Fourier transform to position space can be performed analytically. For the time response $\Phi(t,\vec{x})$ [Eq. (21)] one finds an expanding Gaussian $(2\pi Dt)^{-1} \exp(-r^2/2Dt)$. For the frequency response $\Phi(\omega,\vec{x})$ [Eq. (22)] one finds a modified Bessel function $2\pi |K_0(r\sqrt{i\omega/D})|$, which decays exponentially with r if $0.2 < r\sqrt{\omega/D}$. Our numerical results are very similar to these analytical forms.

The middle panels (c) and (d) show out-of-plane precession from a linearly $\hat{x}$ polarized pump to circular s_z polarization degree. The static response (blue line) shown in panel (d) displays spatial oscillations which are caused by the regularization that we imposed on the diffusion operator at large wave vectors $ql \geqslant 1/\sqrt{2}$. However we have checked that the overall shape and magnitude of the static response are insensitive to the cutoff. In addition, our calculations using other cutoffs show that the frequency response at $T = 5\tau, 20\tau, 80\tau$ is sensitive to the cutoff at small radii $r/\sqrt{DT} < 2$, and other cutoffs not shown here can show substantially larger frequency responses at small r. Outside of this window the frequency response is insensitive to the cutoff. The temporal response is insensitive to the cutoff everywhere.

Panel (c) shows that at $t = 5\tau, 20\tau$ conversion rates can reach and exceed 10^{-1}. Panel (d) shows that similar numbers are obtained from the response to oscillating and static pumps. These numbers decrease substantially at larger times or periods $t, T = 80\tau$, and can be tuned by varying ζ and θ_B. An increased polarization degree can also be obtained by moving to larger radii r, at the cost of reducing the polariton density.

Panels (e) and (f) show the linear s_x polarization degree produced in response to an unpolarized pump. These curves are very similar to the data in panels (c) and (d), but numerically they are about an order of magnitude smaller. This difference in magnitude is caused by the factor of χ, the ratio of the energy splitting to the pump energy E_p, which controls angular variations in the momentum k_F. χ is $1/4\pi \approx 0.08$ in our calculations. χ occurs once in the coupling κ_{0l} of polariton density to circular polarization, signaling that this process requires appreciable angular variations of k_F. χ does not occur at all in the coupling of linear to circular polarization κ_{lc}; therefore panels (e) and (f) are smaller by a factor of χ.

Our time response and frequency response results show that the polarization degree—the ratio of the polarization signal to the density—generally increases with r/r_0. This is a universal trend visible in all of our data, for electrons, polaritons, and holes, and for all values of the model parameters, and is seen in panels (c), (d), (e), and (f). To be clear, the polarization signal itself decreases with r. However its rate of decrease is smaller than that of the number/charge density N, which results in the observed increase in r seen throughout Fig. 4. At large enough r the polarization degree invariably exceeds 1, as seen for example in panel (d). However this unphysical result occurs only when the signal intensity is smaller than the peak value by a factor of 10^{-4} or less; it is not physically measurable. This unphysical result is a mathematical artifact of our diffusive approximation, which does not correctly capture the tails of probability distributions. In the remaining graphs we restrict r to values where the diffusive approximation remains valid.

C. Angular structure in position space

We turn to the polarization's angular distribution in real space, which naturally complements the previous section's analysis of the radial dependence. Our numerical results will confirm the analytical results about the multipole patterns of electrons, polaritons, and holes, and their rotation with ζ. Furthermore, we will show that the multipoles twist into spirals as time progresses, and we will give quantitative results about the signal strengths.

Figure 5 shows the pattern of circular polarization degree $s_z = S_z/I$ which out-of-plane precession produces starting from a linearly polarized pump. Our analytical results indicate that direct conversion of linear to circular polarization in the EY regime requires both a spin-orbit term and a Zeeman splitting, so we make both terms strong with $\theta_B = 5\pi/8$. Here

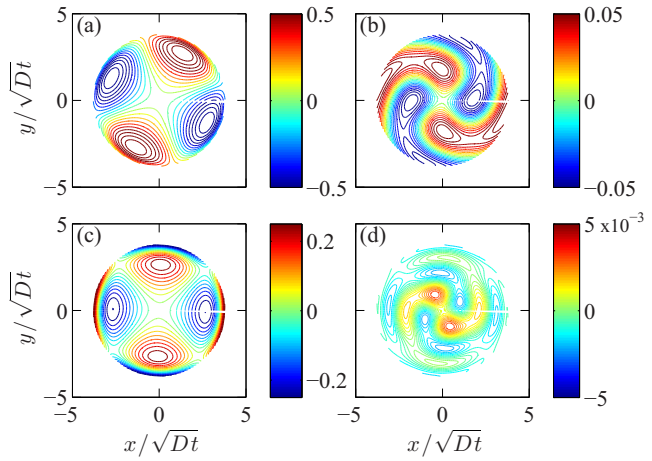

FIG. 5. S_z circular polarization degree in real space, at two values of ζ and two values of time t. The left panels and right panels are $t = 5\tau$ and $t = 20\tau$, respectively, and the upper and lower panels are at $\zeta = 0.25$ and $\zeta = 0.5$, respectively. The pump is linearly $\hat{x}$ polarized. As ζ is increased the polarization's quadrupole distribution rotates. As time increases the quadrupole pattern rotates and deforms into a spiral. $\theta_B = 5\pi/8$, $\chi = \hbar/E_p\tau = 1/4\pi$, $\tau_{\text{decay}} = 50\tau$, and $\tau = 4$ ps.

and in the other radial plots (Figs. 6 and 10) the lattice spacing is $0.2l$ and the system size is $51.2l$. Previous theoretical and experimental articles in the ballistic regime have shown that out-of-plane precession produces a quadrupole pattern with two opposite lobes of positive circular polarization, two negative lobes, and the Langbein cross of zero polarization dividing these lobes [2–8]. Further work, always in the ballistic regime, showed that when a magnetic field is introduced the quadrupole pattern twists into a spiral pattern, with its orientation becoming a function of radius r [8,9]. This rotation occurs because in the ballistic regime the radial position r is

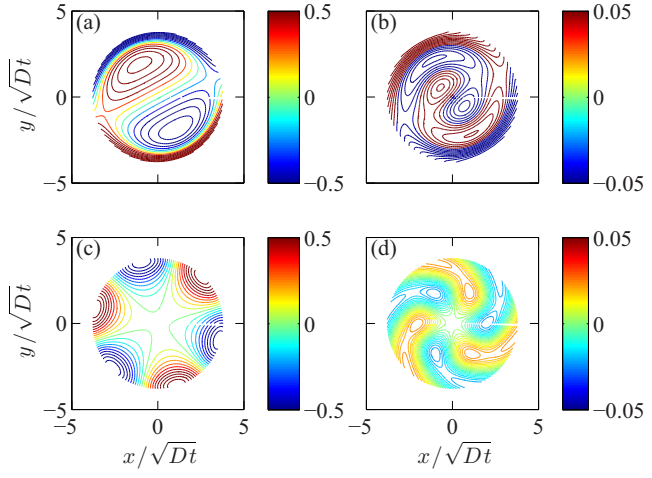

FIG. 6. S_z spin polarization degree in real space, for electrons (upper panels) and holes (lower panels). The left panels and right panels are $t = 5\tau$ and $t = 20\tau$, respectively. The pump is linearly $\hat{x}$ polarized. Electrons show a dipole pattern, and holes show a sextupole pattern. As time increases the pattern rotates and deforms into a spiral in response to the magnetic field. $\zeta = 0.25, \theta_B = 5\pi/8$, $\chi = \hbar/E_p\tau = 1/4\pi, \tau_{\text{decay}} = \infty$, and $\tau = 4$ ps.

proportional to time t, and the external Zeeman field causes in-plane precession at a fixed frequency, which in ballistic fight maps to a precession length. The combination of the quadrupole pattern with spin in-plane precession causes the spiral.

As we discussed earlier, our analytical results for the linear-circular coupling κ_{lc} do predict a quadrupole pattern, and in addition indicate that the quadrupole pattern rotates by $\pi/4$ as the ζ parameter is shifted from the DP regime to the EY regime. The left panels of Fig. 5 show the circular polarization degree at time $t = 5\tau$, at $\zeta = 0.25$ (upper left), and at $\zeta = 0.5$ (lower left). These panels show a clear quadrupole pattern and confirm that the pattern rotates as ζ is changed. Similarly to the ballistic regime, the rotation is caused by in-plane precession superimposed on the multilobe pattern. However—this is a hallmark which can be used to distinguish the diffusive regime from the ballistic regime—no concentric circles are observed in the diffusive regime. Surprisingly, even though there is a Zeeman term the polarization pattern is not twisted into a spiral, unlike previous results in the ballistic regime at $t < \tau$. It seems that the spiral effect does not occur at this time scale. However the right panels of Fig. 5 at $t = 20\tau$ do show clear spiral patterns at both $\zeta = 0.25$ (upper right) and at $\zeta = 0.5$ (lower right.) Appendix B shows that these patterns are mildly sensitive to the cutoff but the main features are cutoff-insensitive. Panel (d) with its very small polarization degree is the exception: its pattern does depend on the cutoff. In summary, the circular polarization pattern deforms from a simple quadrupole pattern to a spiral as time progresses, and its angular orientation is sensitive to both ζ and time t. The most surprising aspect of these results is that no spiral pattern is seen at time $t = 5\tau$, unlike ballistic results. Experimental observation of the spiral pattern's temporal evolution from a simple multipole to a spiral may be a useful means of measuring the scattering time in individual devices.

Figure 6 shows the angular patterns produced by electrons (top panels) and holes (lower panels), which have been little discussed in the previous literature. As expected, electrons display a dipole pattern in real space, and holes show a sextupole pattern. Comparison of the left $t = 5\tau$ and right $t = 20\tau$ panels shows again a time dependence—the initial patterns twist into spirals in response to the magnetic field. In results not shown here, we also have confirmed that the angular orientation of the electron dipole pattern and the hole sextupole pattern rotate in response to variations in ζ, similarly to the polariton's ζ dependence. Probably the most interesting aspect of these results is that the observed real-space spin pattern (dipole, quadrupole, sextupole) is a simple signature that can be used to determine the dominant type of spin-orbit interaction. Moreover, it is likely that in materials with both linear and cubic spin-orbit terms, a numerical analysis of experimental spatial spin distributions could distinguish both terms in the spin-orbit interaction.

D. The polarization's temporal dependence

In the previous sections we analyzed the spin's spatial profile, both its radial and angular dependence. Here we turn to the time dependence of the spin polarization degree, which is determined by the response function $\Phi(t)$, the exponential

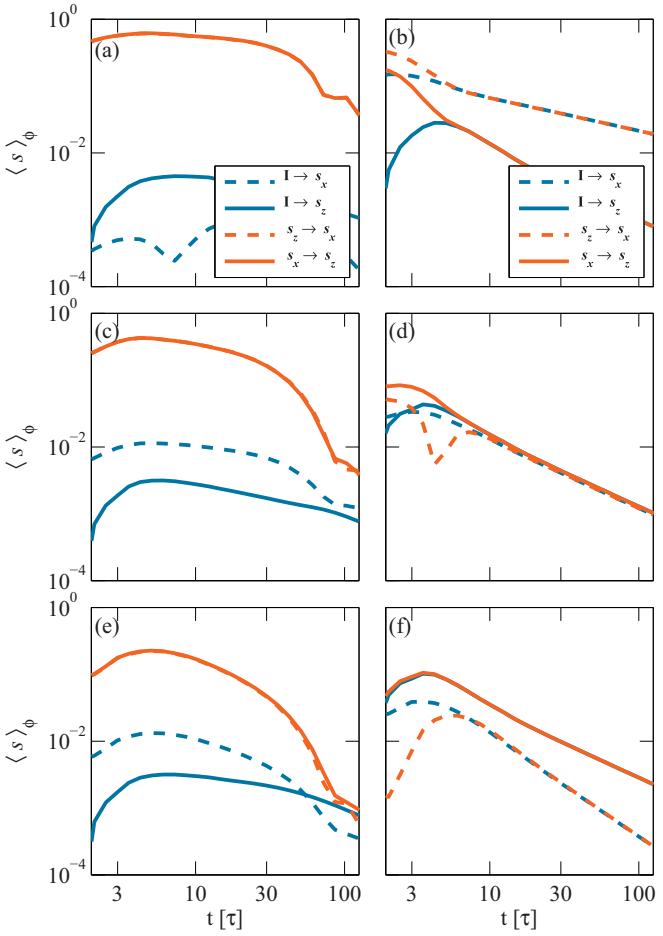

FIG. 7. Temporal dependence in electrons (top), polaritons (middle), and holes (bottom). $\zeta = 0.1$ in the left panels and $\zeta = 4$ in the right panels. Blue lines show the polarization degree produced by an unpolarized pump, and orange lines show the polarization degree caused by out-of-plane precession from polarized pump. Dashed lines show linear s_x polarization degree, and solid lines show circular s_z polarization degree. The data are rms-averaged over the polar angle ϕ. For polaritons $\tau_{\rm decay} = 50\tau$ and for electrons and holes $\tau_{\rm decay} = \infty$. $r/\sqrt{Dt}$ is kept fixed at 3, $\theta_B = 5\pi/8$, $\chi = 1/E_p\tau = 1/4\pi$, $\tau = 4$ ps.

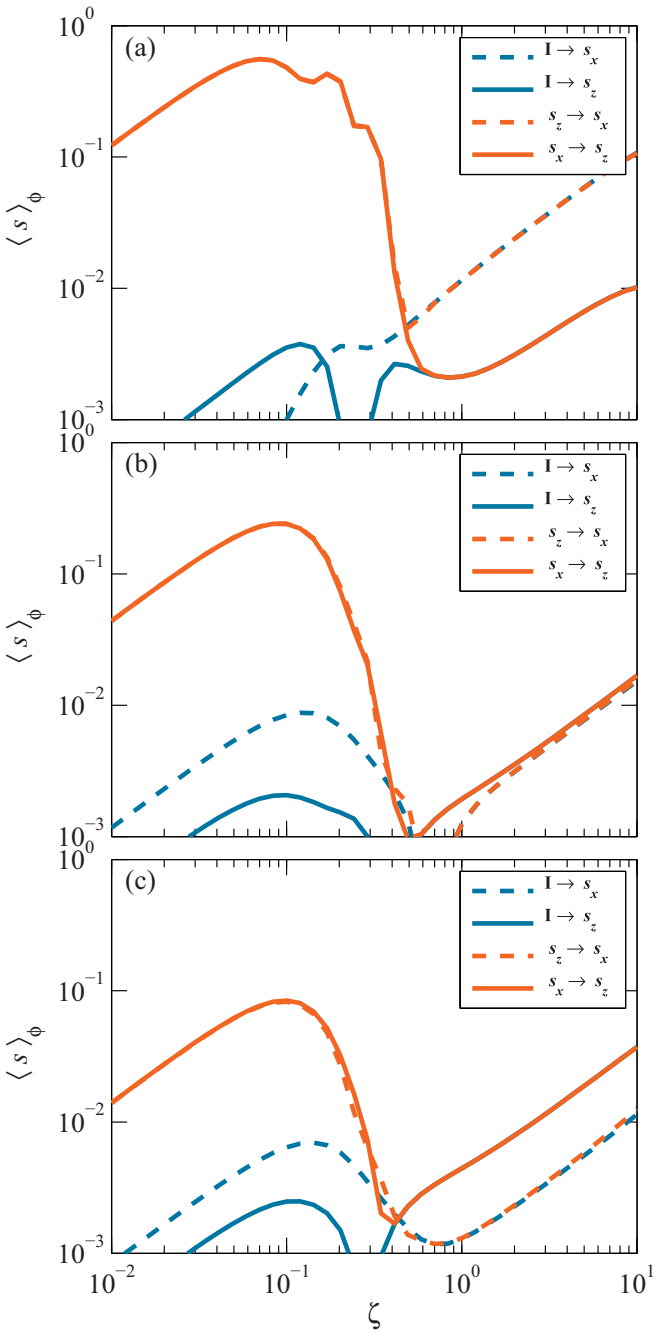

FIG. 8. Dependence on the dimensionless energy splitting $\zeta = l_p/l_{\rm prcsn}$ in electrons (top), polaritons (middle), and holes (bottom). Similarly to Fig. 7, blue lines show the polarization degree produced by an unpolarized pump, and orange lines show the polarization degree caused by out-of-plane precession from a polarized pump. Dashed lines show linear s_x polarization degree, and solid lines show circular s_z polarization degree. The data are rms-averaged over the polar angle ϕ. Here $r/\sqrt{Dt}$ is kept fixed at 3, $t = 20\tau$, $\theta_B = 5\pi/8$, $\chi = 1/E_p\tau = 1/4\pi$, $\tau = 4$ ps.

of the diffusion operator. In Fig. 7 we examine the time dependence of the spin polarization degree of electrons (top panels), polaritons (middle), and holes (lower panels), both in the DP regime (left panels) and in the EY regime (right panels.) In each panel the dashed and solid lines show respectively the linear s_x polarization degree and the circular s_z polarization degree. Blue lines show the s_x, s_z polarization degrees produced by an unpolarized pump, and orange lines show the polarization degrees caused by out-of-plane precession from a polarized pump. The lattice spacing a, both here and in Figs. 8 and 9, is $a = 0.2\,r_0 = 0.2\sqrt{Dt}$. Since the lattice spacing is effectively the size of the spatially localized source pump, this means that we are varying the pump size, with maximum width at $t = 125\,\tau$ of about $a \approx 1.6\,l$. However the effect of this smearing remains small in our plots, which show the spin polarization degree at much large distances $r = 3\,r_0$. The sample width and length are $12.8\,r_0$, large enough to make finite-size effects quite small. We set $\theta_B = 5\pi/8$; i.e., both the Zeeman splitting and the spin-orbit splitting are significant, but not precisely in balance. This allows both in-plane and out-of-plane precession to occur, and therefore gives larger signal strengths than those seen at, for instance, $\theta_B = 0$ or $\theta_B = \pi/2$. At times up $t = 4\tau$ the data may be

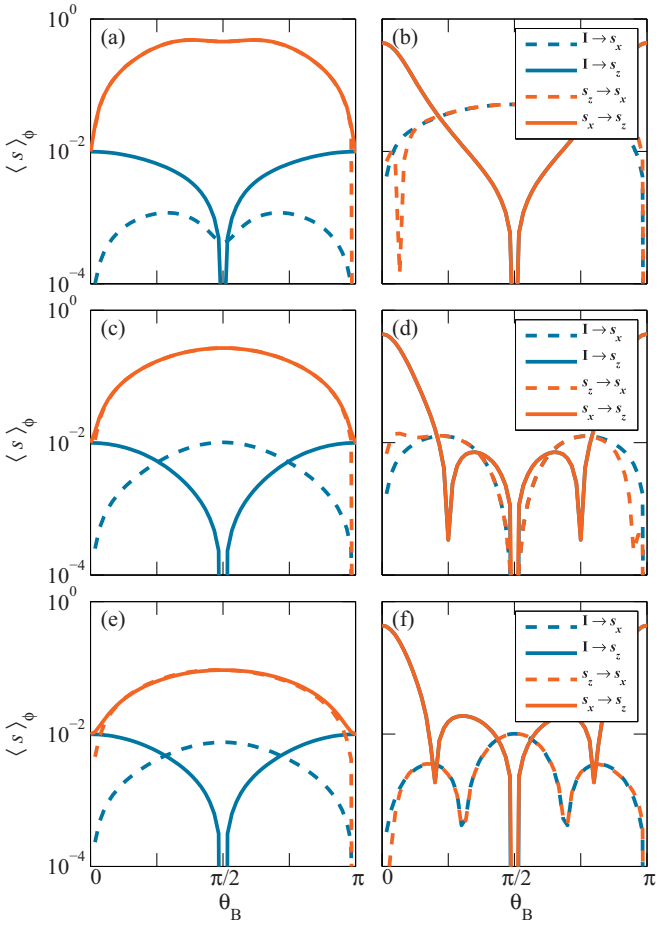

FIG. 9. Dependence on θ_B in electrons (top), polaritons (middle), and holes (bottom). $\zeta = 0.1$ in the left panels and $\zeta = 4$ in the right panels. Blue lines show the polarization degree produced by an unpolarized pump, and orange lines show the polarization degree caused by out-of-plane precession from a polarized pump. Dashed lines show linear s_x polarization degree, and solid lines show circular s_z polarization degree. The data are rms-averaged over the polar angle ϕ. $r/\sqrt{Dt}$ is kept fixed at 3, $t = 80$ ps $= 20\tau$, $\chi = \hbar/E_p\tau = 1/4\pi$, $\tau = 4$ ps.

influenced by ballistic effects which we omitted in our diffusive approximation, and in some cases is sensitive to the cutoff. In particular, with other cutoffs some spin signals are increased. These ballistic/cutoff effects at small times have little effect on the data after $t = 4\tau$.

The spin signals in Fig. 7 generally peak at $t = (4\text{–}8)\tau$ in the DP regime and at $t = (1.75\text{–}6)\tau$ in the EY regime. Obviously this time scale is determined by the scattering time τ. At this time scale, in the DP regime, the out-of-plane precession from an initially polarized pump (orange lines) is dominant, an order of magnitude larger than polarization generated from an unpolarized pump (blue lines). In the EY regime the two processes have similar magnitudes, because any initial polarization decays extremely quickly. The peak polarization degree is greatest for electrons: 61% in the DP regime and 32% in the EY regime. For polaritons it is 43% and 8% respectively for the DP and EY regimes, and for holes it is 23% and 11%. These peak values are independent of the cutoff in the DP regime. They are more sensitive in the EY regime where the peak occurs earlier. As a general trend, the polarization signals are invariably larger in the DP regime than in the EY regime.

Starting at $t = (4\text{–}8)\tau$ in the DP regime and at $t = (1.75\text{–}6)\tau$ in the EY regime, the polarization degree decreases uniformly. At the same time the dashed lines merge with each other, and solid lines also merge with each other. This means that the system loses its memory of the initial polarization, and is sensitive only to the original polariton intensity. The memory loss implies a reversal in the dominant mechanism of spin production: before the memory loss out-of-plane precession is dominant, while after the memory loss it is replaced by spin generation from an unpolarized source.

In the EY regime (right panels) the memory loss completes before $t = 10\tau$, because the spin is tightly locked to the momentum and is randomized at every scattering. In the DP regime (left panels) the memory loss lasts much longer—100τ or longer—because the spin is little affected by scattering and instead is lost by spin-orbit precession around a randomized precession axis. This is consistent with the analytical expectation that in the DP regime the spin relaxation time scales with τ/ξ^2. In our case with $\xi = 0.1$ the memory loss occurs a factor of 10 later than the time of the peak in the polarization degree.

Surprisingly, after memory of the initial polarization is completely lost all polarization degree signals do not decay exponentially, but instead as powers of the inverse time (straight lines on our log-log plots). This power-law decay allows the polarization degree to persist to quite long times: at $t = 100\tau$ the s_z polarization degree for polaritons is 0.5% in the DP regime, and for electrons it is 7%. In the EY regime the $t = 100\tau$ s_x polarization degree is smaller, but is still 2% in the case of electrons.

It is also interesting that after the memory loss the s_x polarization degree is largest for electrons and smallest for holes, because κ_{0l}'s out-of-plane precession between S_x, S_y, and S_z is linear for electrons, quadratic for polaritons, and cubic for holes. In particular, in polaritons the s_x and s_z signals are almost the same because in this case all couplings are quadratic in the momentum. In contrast, the perpendicular s_z polarization degree is roughly the same for all particles, in keeping with the d_{0z} coupling which is the same up to a numerical constant.

E. Dependence on the dimensionless energy splitting ζ

In Fig. 8 we examine the polarization degree's dependence on the energy splitting ζ, which is the ratio of the scattering length l to the precession length l_{prcsn}. We will confirm the analytical results' linear dependence on ζ both in the DP and EY regimes. Going beyond the analytical results, we will reveal the behavior at the transition between DP and EY regimes, give quantitative magnitudes of the signals, and find an interesting feature of polaritons in the EY regime. Again we have set $\theta_B = 5\pi/8$ to allow both in-plane and out-of-plane precession to occur, and to give larger signal strengths. The time is fixed at $t = 20\tau$, long after the first scattering. We plot the same observables seen in Fig. 7, with the same parameter values. The data between $\zeta = 0.25$ and $\zeta = 1$ are mildly dependent on the cutoff, but the qualitative trends are insensitive to the cutoff and to ballistic physics.

The polarization degree signals show a transition which begins near $\zeta = 0.1$ and ends near $\zeta = 1/2$, i.e., at the transition from the DP regime to the EY regime. This transition is controlled by the onset of spin relaxation, which occurs at $t \propto \tau/\zeta^2$ in the DP regime, suggesting that the transition in ζ scales with $t^{-1/2}$. At small $\zeta < 0.1$, i.e., deep in the D'yakonov-Perel' regime, the out-of-plane precession signals (orange lines) are largest and tend to have very similar values. These signals rise steadily with ζ, in agreement with the linear-circular coupling κ_{lc} which is linear in ζ in the DP regime. Production of s_x linear polarization and s_z circular polarization from an unpolarized pump (the blue lines) is smaller. In polaritons and holes this process is linear in ζ, again in agreement with the κ_{0l} and d_{0z} couplings which are linear in ζ.

Near $\zeta = 0.1$ the out-of-plane precession signals (orange lines) reach peak values of 43% in electrons, 24% in polaritons, and 8% in holes. Between $\zeta = 0.1$ and $\zeta = 1/2$ the out-of-plane (orange) signals drop precipitously, and for polaritons and holes the signals from an unpolarized pump (blue lines) also decrease. Near the transition to the EY regime at $\zeta = 0.5$ the solid lines merge with each other, as do also the dashed lines. The mergers indicate that the system loses its memory of the pump polarization; it is sensitive only to the initial pump intensity, not to the initial polarization. This is because at $t = 20\tau$ a system in the EY regime is insensitive to its starting polarization. In the EY regime all polarization signals are linear in ζ, as expected from our couplings $\kappa_{0l}, \kappa_{lc}, d_{0z}$, which are all linear in ζ in the EY regime. We again see that the s_x polarization degree is largest for electrons and smallest for holes, because κ_{0l}'s out-of-plane precession between S_x, S_y, and S_z is linear for electrons, quadratic for polaritons, and cubic for holes. In contrast, the perpendicular s_z polarization degree is roughly the same for electrons, polaritons, and holes. Interestingly, polaritons in the EY regime give almost exactly equal magnitudes for all four of the signals plotted here.

F. Dependence on θ_B, the balance between spin-orbit and Zeeman terms

Figure 9 examines the polarization degree's dependence on the angle θ_B, which describes the balance between the spin-orbit interaction and the Zeeman splitting. When $\theta_B = 0$ there is only a Zeeman splitting and no spin-orbit interaction, and when $\theta_B = \pi/2$ this is reversed. This section confirms the θ_B dependence which we discussed in the analytical section; its main value is to illustrate the analytical results and give quantitative magnitudes. The time is fixed at $t = 20\tau$, long after the first scattering, and the data are almost completely insensitive to cutoff effects. We plot the same observables seen in Figs. 7 and 8, with the same parameter values.

If one flips the sign of both the spin-orbit term and the Zeeman splitting, or equivalently adds π to θ_B, then the polarization signal may change its overall sign but its magnitude must be unchanged. Therefore our plots of the rms-averaged signal are symmetric under $\theta_B \to \theta_B + \pi$, and we plot only the interval $\theta_B = [0,\pi]$. In addition we find that three of the four signals in Fig. 9 are symmetric under flips around $\theta_B = \pi/2$. These signals are independent of the sign of the Zeeman term, which distinguishes between clockwise and counterclockwise precession in the device plane. The one exception occurs in the EY regime, where the linearly polarized s_x response to a circularly polarized s_z pump (dashed orange lines) is not symmetric under flips about $\pi/2$; i.e., it is sensitive to the Zeeman term's sign, as a result of the pump's orientation parallel to the z axis. This sensitivity occurs only if the system retains memory of the original polarization, i.e., either at short times, or even at long times when θ_B is close to zero as seen here. However, even this signal is symmetric under changes at the same time of both the sign of the pump's s_z polarization and also sign of the Zeeman term.

A first examination of Fig. 9 shows that the polarization signals are strongly sensitive to θ_B. In many of our other graphs we have fixed $\theta_B = 5\pi/8$ in order to avoid the deep minima that occur at $\theta_B = 0,\pi/2$, and elsewhere. We also see again that in the EY regime (right panels) the solid lines coincide, and the dashed lines also coincide, except near $\theta_B = 0,\pi$ where S_z is conserved. As noted before, this means that the system has forgotten its initial state.

As discussed earlier, a special feature of electrons is that in the DP regime the conversion from unpolarized pumps to linear polarization scales with $\chi\zeta^3$, a factor of ζ^2 smaller than the conversion to circular polarization, and also a factor of ζ^2 smaller than the same signals in polaritons and holes. In Fig. 9(a) we see that the unpolarized to linear signal (the dashed blue line) is smaller, but not by the factor of $\zeta^2 = 10^{-2}$ that might be expected. The reason is that here we are seeing the result of a two-step process: (a) conversion to circular polarization, and (b) precession from circular to linear polarization. This also explains why the unpolarized to linear signal is zero at $\theta_B = \pi/2$, i.e., when there is no magnetic field.

Broadly speaking, the details of Fig. 9 confirm features of the θ_B dependence which we found in our analysis of the couplings κ_{0l},κ_{lc},d_{0z}. In particular:

(1) No linearly polarized signal is produced when there is no spin-orbit coupling, i.e., at $\theta_B = 0$. This is universal for electrons, polaritons, and holes, and occurs because a Zeeman field oriented along the $\hat{z}$ axis is unable to create a linear polarization, because it is unable break the rotational symmetry in the xy plane.

(2) At $\theta_B = 0$ the absence of a spin-orbit term ensures that the lifetime of circular S_z polarization is infinite. Therefore at $\theta_B = 0$ we find large circular s_z polarization degrees. The s_z magnitude at $\theta_B = 0$ is close to $\chi\zeta = \zeta/4\pi \approx 0.08 \times \zeta$, and is insensitive to ζ and to any initial linear S_x polarization. It is also the same for electrons, polaritons, and holes.

(3) In the DP regime (left panels), regardless of the value of θ_B, a linearly $\hat{x}$ polarized pulse always generates s_z polarization. When there is no spin-orbit coupling, i.e., $\theta_B = 0$, the s_z polarization is generated by conversion from the pump's initial number/charge density, and its magnitude is of order $\chi\zeta$. When there is no magnetic field, i.e., $\theta_B = \pi/2$, the spin-orbit coupling causes out-of-plane precession and produces the s_z polarization. In this case its magnitude reaches 48% in electrons, 27% in polaritons, and 9% in holes.

The most interesting aspects of Fig. 9 are the differences between electrons, polaritons, and holes:

(1) In the EY regime (right panels) polaritons exhibit no polarization signal at all unless there is a Zeeman term, so at $\theta_B = \pi/2$ all signals are zero. This contrasts with electrons and

holes in the EY regime, where a Zeeman term is not necessary for producing an s_x signal, and is required only for producing s_z. This means that for electrons and holes the dashed lines are nonzero at $\theta_B = \pi/2$.

(2) In both the EY and the DP regime an unpolarized pump does not produce a linearly polarized s_x signal unless a magnetic field is introduced, so at $\theta_B = \pi/2$ the solid blue lines are zero.

(3) Setting $\theta_B = \pi/4,\ 3\pi/4$ creates a resonance condition where the Zeeman and spin-orbit terms have precisely the same magnitude, i.e., in polaritons $|b_z| = |\Delta_{SO} k_F^2|$. For polaritons in the EY regime this resonance condition zeros the generation of circular s_z polarization (graphed as solid blue and orange lines), causing sharp dips at $\theta_B = \pi/4,\ 3\pi/4$. Holes in the EY regime also display a resonance effect, with a shifted resonance which occurs at $|b_z| = \sqrt{2}|\Delta_{SO} k_F^3|$. In addition, holes manifest a similar resonance condition in the generation of s_x linear polarization from an unpolarized pump, shown as dashed blue and orange lines. In contrast electrons do not display any resonance at any value of b_z. The resonances shown here may be useful for measurements of the spin-orbit strength in polariton and hole systems in the EY regime.

G. Summary of the numerics

The main value of our numerical results, as opposed to our analytical formulas, is that they offer a clear picture of the spatial spin patterns in these systems, and also of their time evolution. Our spatial data on the number/charge density showed that the frequency response always follows a simple decaying exponential in real space, while the temporal response follows a Gaussian. Moreover, our data showed that changing the time parameter, or indeed any other parameter, has no influence on the number/charge density other than rescaling its exponential or Gaussian profile.

The spin polarization shows much richer behavior. Electrons, polaritons, and holes produce dipole, quadrupole, and sextupole patterns respectively, which provides a very simple and strong diagnostic tool for visually determining the dominant spin-orbit term. Our numerical results confirm that these patterns are clearly visible in the diffusive regime. In real materials the spin-orbit interaction may involve more than one term, for instance both linear and cubic terms, and in this case numerical analysis of experimental data will reveal the relative strength of the spin-orbit terms. Our numerical results also showed that in the presence of a magnetic field, the spin distribution evolves with time from a simple multipole into a spiral. This too will be useful for measuring the scattering time in individual devices. Moreover, we saw that in the diffusive regime there is no pattern of concentric circles around the pump, which allows an unambiguous determination of whether the system is in the diffusive or ballistic regime.

The numerical data also gave us rich information about the time dependence, and told us how large the polarization degree can become. We can break the time evolution into two phases: before and after the time when the system loses memory of its initial polarization. This memory loss occurs at $t \propto \tau/\xi^2$ in the DP regime, and before $t = 10\,\tau$ in the EY regime. Before memory loss occurs, the dominant source of spin dynamics is out-of-plane precession which converts S_x, S_y spin to S_z spin, and vice versa. With an optimal value of the dimensionless spin splitting $\xi = 0.1$, this process yields maximum polarization degrees of 23–61% in the DP regime at around $t = 4$–8τ. In the EY regime at $\xi = 4$ the maximum polarization degrees are between 8% and 32%, occur at $t = 1.75$–6τ, and grow linearly with ξ. These maximum values are largest for electrons. After the maximum, spin relaxation causes a steady decrease in the polarization degree.

As the system loses its memory of the initial polarization, the dominant mechanism producing spin polarization changes from spin precession to direct conversion from the number/charge density. In this phase the spin polarization degree decreases as a power of the time, and in particular the linear s_x polarization degree is largest for electrons and weakest for holes. The circular polarization degree is about the same for all three particles. Even at $t = 100\tau$ the polarization degree for electrons can remain as high as 7% in the DP regime, or 2% in the EY regime.

Lastly, our numerical results about the ζ dependence gave the transition between DP and EY regimes (not shown in the analytical results), and gave an optimal value of ζ. Our θ_B results largely illustrated and confirmed the analytical results on this parameter.

VI. DISCUSSION AND CONCLUSIONS

After proper rescaling of time and distance, in the diffusive regime, spatially homogeneous distributions of electrons, polaritons, and holes act identically. They all have the same spin relaxation times and the same spin precession rates, and in all cases their number charge/density shows the same spatial profile spreading away from the pump. This is perhaps disappointing, since one might wish to see at this level some clear difference between the bosonic polariton and the fermionic electron and hole, similarly to the difference between Bose-Einstein condensation and fermionic repulsion that is seen at large particle densities. At small particle densities, in the noninteracting limit, the perturbative treatment utilized here shows no such signal. There is still some possibility that a Berry phase or other quantum effect could distinguish between the three particles, but there is no such effect even in the weak localization signal, which is determined by relaxation times that are mathematically identical to the spin relaxation times calculated here. Any such quantum effect will be rather subtle.

However, using a spatially localized pump will immediately reveal very large differences between the three particles. The most important difference is their multipole spatial pattern, which has two lobes for electrons, four for polaritons, and six for holes. This spatial distribution provides an unambiguous signal to experimentalists for determining immediately which spin-orbit term is dominant, and also provides the raw data for quantitative analysis of the strengths of competing spin-orbit terms. It is a very strong signal: if the pump is initially linearly polarized, then in the DP regime a multipole pattern in the circular polarization can be observed, with a polarization degree of up to 23–61%, and can persist for long times. In the EY regime the same process can produce between 8% and 32%

polarization degree. Production of linear polarization from an unpolarized pump also produces appreciable multipole patterns.

The three particles also differ in their response to a perpendicular magnetic field. For electrons and holes, in the EY regime an unpolarized pump always produces a multipole pattern of linear polarization, regardless of the magnetic field strength. In contrast for polaritons in the EY regime no linear polarization is generated from an unpolarized pump unless there is a magnetic field. Moreover in the EY regime polaritons and holes manifest a resonance, where no circular S_z polarization is generated from an unpolarized pump, at a specific field strength that matches the spin-orbit strength. The resonance occurs at numerically different field strengths for different particles, and varies with spin-orbit strength. This will allow experimentalists both to measure the spin-orbit strength and to confirm again whether the particle is an electron, polariton, or hole.

The last major difference between the three particles is in the magnitude of multipole pattern that is produced. In electrons, polaritons, and holes this scales respectively with the first, second, and third power of the scattering length. In the diffusive regime studied here the scattering length is small compared to the experimental length scale, so the multipole is strongest for electrons and weakest for holes. One interesting way of testing this trend is to compare, at long times, the linear and circular polarization produced from an unpolarized pump. The circular signal is rotationally symmetric and its magnitude is about the same for all three particles. In the case of electrons the circular signal should be smaller than the linearly polarized signal, in the case of holes this is reversed, and in the case of polaritons the two signals have very similar magnitudes.

ACKNOWLEDGMENTS

This work was supported by FP7 ITM "NOTEDEV", Rannis project "Bose, Fermi, and Hybrid Systems for Spintronics.", Tier 2 project "Polaritons for Novel Device Applications" and Russian Target Federal Program, project 14.587.21.0020. A.P. thanks the University of Iceland for hospitality. We thank T. Liew and S. Morina for insightful discussions.

APPENDIX A: THE DIFFUSON IN THE GENERAL CASE, FOR ANY VALUE OF ζ, AND FOR LINEAR, QUADRATIC, AND CUBIC SPIN-ORBIT TERMS

In this article we report on spin dynamics for the following Hamiltonian:

$$H = \frac{k^2}{2m} + b_z\sigma_z + \Delta_{SO}k^N\begin{bmatrix} 0 & e^{-\imath N\phi_k} \\ e^{\imath N\phi_k} & 0 \end{bmatrix} = \frac{k^2}{2m} + b_z\sigma_z + \Delta_{SO}\begin{bmatrix} 0 & (k_x-\imath k_y)^N \\ (k_x+\imath k_y)^N & 0 \end{bmatrix}. \tag{A1}$$

We consider the cases of linear $N=1$, quadratic $N=2$, and cubic $N=3$ spin-orbit interactions. We assume that the impurities conserve the (pseudo)spin quantum number; if this constraint is relaxed then our results on the matrix structure of the diffuson will change substantially.

For the Hamiltonian H, we obtain the diffuson D^{-1}:

$$\tau D^{-1} = \tau\partial_t + \begin{bmatrix} (ql)^2/2 & 0 & 0 & d_{0z,N}(ql)^2/2 \\ 0 & \tau/\tau_{xx} + d_{xx,N}(ql)^2/2 & \tau/\tau_{xy} + d_{xy,N}(ql)^2/2 & 0 \\ 0 & -\tau/\tau_{xy} - d_{yx,N}(ql)^2/2 & \tau/\tau_{xx} + d_{yy,N}(ql)^2/2 & 0 \\ d_{0z,N}(ql)^2/2 & 0 & 0 & \tau/\tau_{zz} + d_{zz}(ql)^2/2 \end{bmatrix}$$
$$-(\imath ql)^N\begin{bmatrix} 0 & \gamma_N\cos N\theta_q & \gamma_N\sin N\theta_q & 0 \\ \gamma_N\cos N\theta_q & 0 & 0 & f_N\cos N\theta_q - g_N\sin N\theta_q \\ \gamma_N\sin N\theta_q & 0 & 0 & f_N\sin N\theta_q + g_N\cos N\theta_q \\ 0 & f_N\cos N\theta_q + g_N\sin N\theta_q & f_N\sin N\theta_q - g_N\cos N\theta_q & 0 \end{bmatrix},$$

$$\tau/\tau_{xy} = 2C\frac{\zeta}{1+4\zeta^2},\ \tau/\tau_{xx} = 2(1+C^2)\frac{\zeta^2}{1+4\zeta^2},\ \tau/\tau_{zz} = 4S^2\frac{\zeta^2}{1+4\zeta^2},\ d_{zz} = \left[C^2 + S^2\frac{1-12\zeta^2}{(1+4\zeta^2)^3}\right],$$

$$d_{xy,2} = d_{xy,3} = d_{yx,2} = d_{yx,3} = \frac{2C\zeta(-3+4\zeta^2)}{(1+4\zeta^2)^3},$$

$$d_{xx,2} = d_{yy,2} = d_{xx,3} = d_{yy,3} = \frac{1}{2}\left[S^2 + (2-S^2)\frac{1-12\zeta^2}{(1+4\zeta^2)^3}\right],$$

$$d_{xx,1} = d_{xx,2} + e\cos(2\theta_q),\ d_{yy,1} = d_{yy,2} - e\cos(2\theta_q),\ d_{xy,1} = d_{xy,2} + e\ \sin(2\theta_q),\ d_{yx,1} = d_{yx,2} - e\ \sin(2\theta_q),$$

$$e = \frac{2\zeta^2S^2(3+6\zeta^2+8\zeta^4)}{(1+4\zeta^2)^3},$$

$$d_{0z,N} = -\chi\zeta C^3 + (N-1)\chi\zeta CS^2 - 1/(1+4\zeta^2)^2 \times \chi\zeta CS^2\,N,$$

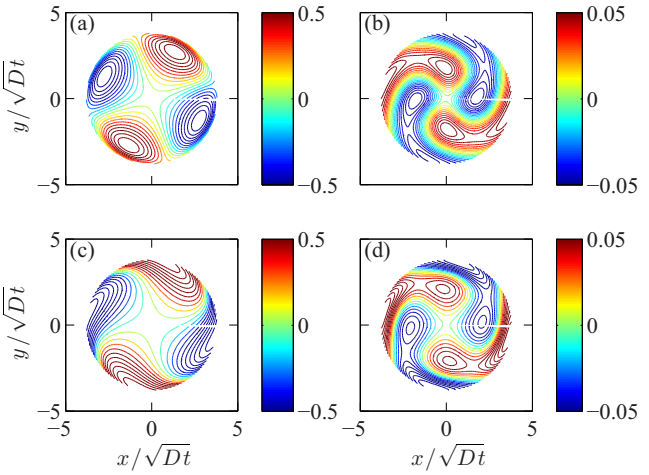

FIG. 10. Cutoff dependence of our results. Circular S_z spin polarization degree in real space, for cutoff A (upper panels) and cutoff B (lower panels). The left panels and right panels are $t = 5\tau$ and $t = 20\tau$ respectively. The pump is linearly $\hat{x}$ polarized. $\zeta = 0.25$, $\theta_B = 5\pi/8$, $\chi = \hbar/E_p\tau = 1/4\pi$, and $\tau = 4$ ps.

$$\begin{aligned}
\gamma_N &= \chi\zeta S \times \{(1+C^2)/4, C^2/2, (3/16)(2C^2 - S^2)\} \\
&\quad + \chi\zeta S/(1+4\zeta^2)^N \times (1+C^2) \times \{-1/4, -1/2, -(9/16)(1-4\zeta^2/3)\}, \\
f_N &= \frac{CS\zeta^2}{(1+4\zeta^2)^{N+1}} \times \{-(6+8\zeta^2), 6+12\zeta^2+16\zeta^4, -(5+10\zeta^2+32\zeta^4+32\zeta^6)\}, \\
g_N &= \frac{\zeta S}{(1+4\zeta^2)^{N+1}} \times \{2, (-3+4\zeta^2)/2, 1-4\zeta^2\}. \qquad \text{(A2)}
\end{aligned}$$

The constant contributions to the matrix $\tau/\tau_{xx}, \tau/\tau_{zz}, \tau/\tau_{xy}$, which determine the evolution of a spatially uniform distribution, are independent of N. The diffusion constant d_{zz} is also independent of N.

As described earlier, $S = \sin(\theta_B) = \Delta_{SO}k_F^N/\sqrt{(\Delta_{SO}k_F^N)^2 + b_z^2}$ and $C = \cos(\theta_B) = b_z/\sqrt{(\Delta_{SO}k_F^N)^2 + b_z^2}$ describe the relative strength of the spin-orbit coupling $\Delta_{SO}k_F^N$ and the Zeeman term b_z.

APPENDIX B: NUMERICAL RESULTS ON THE CUTOFF DEPENDENCE

As discussed in the text, some of our numerical results are sensitive to physics at length scales shorter than the scattering length l, i.e., ballistic physics. These numerical results are changed by our perturbative expansion of the response function in powers of ql. We have tested our results by calculating them in three different ways:

Cutoff A. At small wave number $0.5 > (ql)^2$ we use the formulas presented in Appendix A. At large wave number $(ql)^2 > 2$ we set κ_{0l}, κ_{lc}, and D_{0z} to zero, and we set $\Delta = (ql)^2/2$. At intermediate wave numbers $2 > (ql)^2 > 0.5$ we perform a linear interpolation of $\kappa_{0l}, \kappa_{lc}, D_{0z}, \Delta$ between these two cases.

Cutoff B. At small wave number $0.5 > (ql)^2$ we use the formulas presented in Appendix A. At large wave number $(ql)^2 > 2$ we use the expressions for the D'yakonov-Perel' limit, as listed in Eqs. (26), (27), (28), (29), and (31). At intermediate wave numbers $2 > (ql)^2 > 0.5$ we perform a linear interpolation between these two cases.

Cutoff C. We use only the formulas presented in Appendix A, without any changes, for all values of ql.

Since cutoff C leaves the analytical formulas unchanged, it retains the original instability near $\zeta = 1/2$. Both cutoffs A and B do not show instability for electrons and polaritons. Holes are stable only with cutoff A and are unstable with both cutoffs B and C, presumably because our analytical expressions for holes include cubic $(ql)^3$ terms which are more unstable than the quadratic terms seen in electrons and polaritons.

Figure 10 illustrates the differences between two cutoffs. The upper panels are obtained using cutoff A, and the lower panels with cutoff B. Very similar patterns and magnitudes are seen, with some mild distortions. We have performed similar comparisons, with all three cutoffs, for all of our real-space data. In cases where different cutoffs give different results, we have discussed this in the main text.

APPENDIX C: DERIVATION OF THE κ_{0l} AND d_{0z} COUPLINGS

Here we report the details of our derivation of the coupling κ_{0l} between charge and in-plane S_x, S_y spin, and also in the coupling d_{0z} between charge and out-of-plane S_z spin. We have performed the calculation systematically in a very general MATHEMATICA script which allows calculation to quite high orders in the various small parameters. However here we do not discuss the script,

and instead show in analytical formulas how the derivation develops. We compute the d_{0z} coupling which is equal to $-I_{03}$, and the κ_{0l} coupling which is equal $-I_{01}$ and $-I_{02}$, where I_{ij} is the scattering operator. We begin with Eq. (24), which writes I_{ij} as the integral

$$I_{ij} = \frac{\hbar}{4\pi\nu\tau}\int d\vec{k}\,\mathrm{Tr}[G^A(\vec{k}-\vec{q}/2,E_p)\sigma_i G^R(\vec{k}+\vec{q}/2,E_p)\sigma_j]. \tag{C1}$$

Here G^A and G^R are the disorder-averaged single-particle Green's functions, $\vec{q}$ is the diffuson wave vector, and ν is the density of states. The trace is taken over the spin indices of G^A,G^R,σ_i, and σ_j, which are all 2×2 matrices in (pseudo)spin space. The advanced and retarded Green's functions can be resolved into separate contributions from the two spin states $s=\pm 1$, which have energies $E(s,\vec{k})$:

$$\begin{aligned} G^{A,R}(\vec{k},E) &= \frac{1}{2}\sum_s \frac{1+s\vec{X}(\vec{k})\cdot\vec{\sigma}}{E-E(s,\vec{k})\mp\imath\hbar/2\tau}, \quad \vec{\sigma}=[\sigma_x,\sigma_y,\sigma_z]^T, \\ X_1 &= \frac{\Delta_{SO}\,\mathrm{Re}[(k_x+\imath k_y)^N]}{\sqrt{(\Delta_{SO}|k|^N)^2+b_z^2}}, \quad X_2 = \frac{\Delta_{SO}\,\mathrm{Im}[(k_x+\imath k_y)^N]}{\sqrt{(\Delta_{SO}|k|^N)^2+b_z^2}}, \quad X_3 = \frac{b_z}{\sqrt{(\Delta_{SO}|k|^N)^2+b_z^2}}. \end{aligned} \tag{C2}$$

Performing the trace and applying the identity $(ab)^{-1}=(a^{-1}-b^{-1})(b-a)^{-1}$ quickly obtains

$$\begin{aligned} d_{0i} &= -I_{0i} = -\frac{\hbar}{8\pi\nu\tau}\int d\vec{k}\sum_{s,\acute{s}}[s\,X_i(\vec{k}-\vec{q}/2)+\acute{s}\,X_i(\vec{k}+\vec{q}/2)]Y, \\ Y &= \frac{1}{E_p-E(s,\vec{k}-\vec{q}/2)-\imath\hbar/2\tau}\frac{1}{E_p-E(\acute{s},\vec{k}+\vec{q}/2)+\imath\hbar/2\tau} \\ &\approx \frac{\pi\tau}{\hbar}\left[\frac{\delta(E_p-E(s,\vec{k}-\vec{q}/2))}{1+\imath\tau[E(\acute{s},\vec{k}+\vec{q}/2)-E_p]/\hbar}+\frac{\delta(E_p-E(\acute{s},\vec{k}+\vec{q}/2))}{1+\imath\tau[E_p-E(s,\vec{k}-\vec{q}/2)]/\hbar}\right]. \end{aligned} \tag{C3}$$

In the last line we replaced $[E_p-E(s,\vec{k}-\vec{q}/2)-\imath\hbar/2\tau]^{-1}$ by its imaginary part, which is taken to be the Dirac delta function $\imath\pi\delta(E_p-E(s,\vec{k}-\vec{q}/2))$. This standard approximation is justified if the scattering time is long compared to the kinetic time scale, i.e., $\frac{\hbar}{E_p\tau}\propto\chi\ll 1$. Physically it means that we concern ourselves only with processes that occur on the elastic scattering circle for polaritons, or on the Fermi surface for electrons and holes. After these steps the scattering time τ occurs only in the denominator of Y. Powers of dimensionless energy splitting $\zeta=E_{\mathrm{prcsn}}\tau/\hbar$, because they contain τ, can come only from the denominator of Y.

Multiplying $[s\,X_i(\vec{k}-\vec{q}/2)+\acute{s}\,X_i(\vec{k}+\vec{q}/2)]$ by the two terms in Y and making appropriate shifts $\vec{k}\to\vec{k}\pm\vec{q}/2$ obtains

$$\begin{aligned} d_{0i} = &-\frac{1}{8\nu}\int d\vec{k}\sum_{s,\acute{s}} s\left[\frac{X_i(\vec{k})\,\delta(E_p-E(s,\vec{k}))}{1+\imath\tau[E(\acute{s},\vec{k}+\vec{q})-E(s,\vec{k})]/\hbar}+\frac{X_i(\vec{k}-\vec{q})\,\delta(E_p-E(\acute{s},\vec{k}))}{1+\imath\tau[E(\acute{s},\vec{k})-E(s,\vec{k}-\vec{q})]/\hbar}\right] \\ &-\frac{1}{8\nu}\int d\vec{k}\sum_{s,\acute{s}} \acute{s}\left[\frac{X_i(\vec{k}+\vec{q})\,\delta(E_p-E(s,\vec{k}))}{1+\imath\tau[E(\acute{s},\vec{k}+\vec{q})-E(s,\vec{k})]/\hbar}+\frac{X_i(\vec{k})\,\delta(E_p-E(\acute{s},\vec{k}))}{1+\imath\tau[E(\acute{s},\vec{k})-E(s,\vec{k}-\vec{q})]/\hbar}\right]. \end{aligned} \tag{C4}$$

At this point we expand the X_i functions in powers of $\vec{q}$. Each power of $\vec{q}$ is implicitly accompanied by a power of $1/k_F$, and after a simple manipulation gives a power of $\chi\,ql$, where χ is the dimensionless disorder strength and is a small parameter. Since there are no compensating τ's in X_i, χ can be taken at face value as a small parameter, and we expand only to leading order in χ. In the d_{0i} elements of the diffuson the leading order has a single power of χ, while all other elements of the D are nonzero at zeroth order in χ. Therefore we write

$$X_i(\vec{k}+\vec{q}) = X_i(\vec{k})+\vec{q}\cdot\vec{\nabla}X_i(\vec{k}). \tag{C5}$$

We decompose the diffuson into two parts, a part d_{0i}^0 originating in $X_i(\vec{k})$, and another part d_{0i}^ζ originating in the gradient $\vec{\nabla}X_i(\vec{k})$:

$$\begin{aligned} d_{0i} &= d_{0i}^0+d_{0i}^\zeta, \\ d_{0i}^0 &= -\frac{1}{8\nu}\int d\vec{k}\sum_{s,\acute{s}}(s+\acute{s})\left[\frac{X_i(\vec{k})\,\delta(E_p-E(s,\vec{k}))}{1+\imath\tau[E(\acute{s},\vec{k}+\vec{q})-E(s,\vec{k})]/\hbar}+\frac{X_i(\vec{k})\,\delta(E_p-E(\acute{s},\vec{k}))}{1+\imath\tau[E(\acute{s},\vec{k})-E(s,\vec{k}-\vec{q})]/\hbar}\right], \\ d_{0i}^\zeta &= -\frac{1}{8\nu}\int d\vec{k}\sum_{s,\acute{s}}\left[s\frac{-\vec{q}\cdot\vec{\nabla}X_i(\vec{k})\,\delta(E_p-E(\acute{s},\vec{k}))}{1+\imath\tau[E(\acute{s},\vec{k})-E(s,\vec{k}-\vec{q})]/\hbar}+\acute{s}\frac{\vec{q}\cdot\vec{\nabla}X_i(\vec{k})\,\delta(E_p-E(s,\vec{k}))}{1+\imath\tau[E(\acute{s},\vec{k}+\vec{q})-E(s,\vec{k})]/\hbar}\right]. \end{aligned} \tag{C6}$$

This decomposition is physically significant. The $s \neq \acute{s}$ terms make an exactly null contribution to d^0_{0i}, so a little rearrangement obtains

$$\begin{aligned} d^0_{0i} &= -\frac{1}{4\nu}\int d\vec{k}\sum_s s\left[\frac{X_i(\vec{k})\,\delta(E_p - E(s,\vec{k}))}{1+\imath\tau[E(s,\vec{k}+\vec{q}) - E(s,\vec{k})]/\hbar} + \frac{X_i(\vec{k})\,\delta(E_p - E(s,\vec{k}))}{1+\imath\tau[E(s,\vec{k}) - E(s,\vec{k}-\vec{q})]/\hbar}\right] \\ &= -\frac{1}{2\nu}\int d\vec{k}\sum_s s\frac{X_i(\vec{k})\,\delta(E_p - E(s,\vec{k}))}{1+\imath\tau\vec{q}\cdot\nabla E(s,\vec{k})/\hbar}. \end{aligned} \tag{C7}$$

In the last line we have expanded in powers of $\vec{q}$, following the same argument as before. In contrast to the previous expansion, the first term in the present expansion is matched by a factor of τ, so it actually scales as ql without any powers of χ. Since the denominator subtracts $E(s,\vec{k})$ from $E(s,\vec{k}+\vec{q})$ and therefore has no powers of the spin-orbit splitting, d^0_{0i} can contain no powers of $(1+4\zeta^2)^{-1}$. Because of the guarding factor of s multiplying the sum, nonzero contributions can be obtained only from a dependence on the spin index s of the Dirac delta function, or of X_i, or of $\nabla E(s,\vec{k})$. Physically, variations in the Dirac delta function with s reflect a difference between the density of states on the spin up $s=+1$ Fermi surface and the density of states on the spin down Fermi surface. Similarly, variations in $\nabla E(s,\vec{k})$ correspond to differences in the Fermi velocity on the two Fermi surfaces, and variations in X_i to differences in the spin-orbit interaction's angular orientation on the two surfaces. In order to analyze these effects, it is necessary to calculate the spin splitting of the two $s=\pm1$ Fermi surfaces, as a function of the angular variable ϕ_k. It is sufficient to obtain them to first order in the ratio of the spin splitting to the Fermi energy, $E_{\mathrm{prcsn}}/E_p = \chi\zeta$. After doing so, we obtain in the case of the Rashba interaction

$$\begin{aligned} d^0_{01} &= -\frac{1}{2\nu}\int d\vec{k}\sum_s s\frac{X_1(\vec{k})\,\delta(E_p - E(s,\vec{k}))}{1+\imath\tau\vec{q}\cdot\nabla E(s,\vec{k})/\hbar} \\ &= -\int\frac{d\phi_k}{2\nu}\sum_s s\,\rho(s,\phi_k)\frac{X_1(s,\phi_k)}{1+\imath\tau\vec{q}\cdot\nabla E(s,\phi_k)/\hbar}, \\ \rho(s,\phi) &= \int k\,dk\,\delta(E_p - E(s,\vec{k})) = \frac{k_F^2}{2E_F}[1-\chi\zeta s\sin^2(\theta_B)/2], \\ \nu &= \sum_s\int_0^{2\pi} d\phi\rho(s,\phi) = 4\pi\frac{k_F^2}{2E_F}, \\ X_1(s,\phi) &= \cos(\theta_k)\sin(\theta_B)[1 - s\chi\zeta\cos^2(\theta_B)/2], \\ \frac{1}{1+\imath\tau\vec{q}\cdot\nabla E(s,\phi_k)/\hbar} &= 1 - \imath ql\cos(\theta_k-\theta_q) + \imath ql\chi\zeta\cos^2(\theta_B)s\cos(\theta_k-\theta_q)/2, \\ d^0_{01} &= -\imath q_x l\chi\zeta\sin(\theta_B)[1+\cos^2(\theta_B)]/4. \end{aligned} \tag{C8}$$

We have automated this perturbative calculation, and also the calculation of d^ζ, with MATHEMATICA, which facilitates the calculation of all matrix elements to high orders.

We now turn to the other contribution, d^ζ_{0i}. Exchanging $s,\acute{s}$ in the second term and then expanding in powers of $\vec{q}\cdot\nabla E \propto ql$ produces

$$\begin{aligned} d^\zeta_{0i} &= -\frac{1}{8\nu}\int d\vec{k}\sum_{s,\acute{s}} s\,\vec{q}\cdot\vec{\nabla}X_i(\vec{k})\,\delta(E_p - E(\acute{s},\vec{k}))\left[\frac{-1}{1+\imath\tau[E(\acute{s},\vec{k}) - E(s,\vec{k}-\vec{q})]/\hbar} + \frac{1}{1+\imath\tau[E(s,\vec{k}+\vec{q}) - E(\acute{s},\vec{k})]/\hbar}\right] \\ &= -\frac{1}{8\nu}\int d\vec{k}\sum_{s,\acute{s}} s\,\vec{q}\cdot\vec{\nabla}X_i(\vec{k})\,\delta(E_p - E(\acute{s},\vec{k}))\sum_M\sum_\pm\frac{\mp[-\imath\tau\vec{v}_F(\vec{k})\cdot\vec{q}]^{M-1}}{\{1\pm\imath\tau[E(\acute{s},\vec{k}) - E(s,\vec{k})]/\hbar\}^M}. \end{aligned} \tag{C9}$$

The $\vec{q}\cdot\vec{\nabla}X_i(\vec{k})$ multiplying the entire expression is proportional to $\chi\,ql$, which guarantees a power of χ. Therefore all other expressions must remain at zeroth order in χ, allowing us to neglect the spin splitting effects on the density of states, Fermi velocity, and X_i, which are so important for determining d^0_{0i}. In this approximation the Fermi surface becomes a simple circle and the $d\vec{k}$ turns into a simple angular integral over ϕ_k. Moreover, the factor of s multiplying everything guarantees that the two $s=\acute{s}$ contributions sum to zero, leaving us with

$$d^\zeta_{0i} = -\int\frac{d\phi_k}{16\pi}\,\vec{q}\cdot\vec{\nabla}X_i(\vec{k})\sum_M[-\imath\tau\vec{v}_F(\vec{k})\cdot\vec{q}]^{M-1}\sum_\pm\sum_s\frac{\mp s}{(1\mp\imath s2\zeta)^M}. \tag{C10}$$

For the couplings to in-plane spins, d^ζ_{01} and d^ζ_{02}, the angular integration selects the $M=N$ term, where $N=1,2,3$ for electrons, polaritons, and holes. For the coupling to out-of-plane spins, d^ζ_{03}, the angular integral selects the $M=2$ term. For $N=1,2,3$ the

last factor $\sum_{\pm}\sum_{s}\frac{\mp s}{(1\mp \imath s 2\zeta)^M}$ sums to

$$\frac{-\imath 8\zeta}{(1+4\zeta^2)^N}\times(1,2,3(1-4\zeta^2/3)). \tag{C11}$$

If one performs the remaining angular integral and sums d^0_{0i},d^{ζ}_{0i}, then one obtains the charge-spin couplings reported in this article.

[1] I. Shelykh, A. Kavokin, Y. G. Rubo, T. Liew, and G. Malpuech, Semicond. Sci. Technol. **25**, 013001 (2010).

[2] A. Kavokin, G. Malpuech, and M. Glazov, Phys. Rev. Lett. **95**, 136601 (2005).

[3] C. Leyder, M. Romanelli, J. P. Karr, E. Giacobino, T. Liew, M. Glazov, A. Kavokin, G. Malpuech, and A. Bramati, Nat. Phys. **3**, 628 (2007).

[4] W. Langbein, I. Shelykh, D. Solnyshkov, G. Malpuech, Y. Rubo, and A. Kavokin, Phys. Rev. B **75**, 075323 (2007).

[5] T. C. H. Liew, C. Leyder, A. V. Kavokin, A. Amo, J. Lefrère, E. Giacobino, and A. Bramati, Phys. Rev. B **79**, 125314 (2009).

[6] A. Amo, T. C. H. Liew, C. Adrados, E. Giacobino, A. V. Kavokin, and A. Bramati, Phys. Rev. B **80**, 165325 (2009).

[7] E. Kammann, T. C. H. Liew, H. Ohadi, P. Cilibrizzi, P. Tsotsis, Z. Hatzopoulos, P. G. Savvidis, A. V. Kavokin, and P. G. Lagoudakis, Phys. Rev. Lett. **109**, 036404 (2012).

[8] S. Morina, T. C. H. Liew, and I. A. Shelykh, Phys. Rev. B **88**, 035311 (2013).

[9] A. A. High, A. T. Hammack, J. R. Leonard, S. Yang, L. V. Butov, T. Ostatnický, M. Vladimirova, A. V. Kavokin, T. C. H. Liew, K. L. Campman *et al.*, Phys. Rev. Lett. **110**, 246403 (2013).

[10] T. Dollinger, M. Kammermeier, A. Scholz, P. Wenk, J. Schliemann, K. Richter, and R. Winkler, Phys. Rev. B **90**, 115306 (2014).

[11] V. E. Sacksteder and B. A. Bernevig, Phys. Rev. B **89**, 161307 (2014).

[12] R. Winkler, Phys. Rev. B **62**, 4245 (2000).

[13] D. M. Whittaker, P. Kinsler, T. A. Fisher, M. S. Skolnick, A. Armitage, A. M. Afshar, M. D. Sturge, and J. S. Roberts, Phys. Rev. Lett. **77**, 4792 (1996).

[14] B. Nelsen, G. Liu, M. Steger, D. W. Snoke, R. Balili, K. West, and L. Pfeiffer, Phys. Rev. X **3**, 041015 (2013).

[15] M. Steger, G. Liu, B. Nelsen, C. Gautham, D. W. Snoke, R. Balili, L. Pfeiffer, and K. West, Phys. Rev. B **88**, 235314 (2013).

[16] M. Steger, C. Gautham, D. W. Snoke, L. Pfeiffer, and K. West, Optica **2**, 1 (2015).

[17] C. Antón, T. C. H. Liew, J. Cuadra, M. D. Martín, P. S. Eldridge, Z. Hatzopoulos, G. Stavrinidis, P. G. Savvidis, and L. Viña, Phys. Rev. B **88**, 245307 (2013).

[18] M. Sakai, Y. Inose, T. Ohtsuki, K. Ema, K. Kishino, and T. Saiki, Jpn. J. Appl. Phys. **53**, 030301 (2014).

[19] T. Jacqmin, I. Carusotto, I. Sagnes, M. Abbarchi, D. D. Solnyshkov, G. Malpuech, E. Galopin, A. Lemaître, J. Bloch, and A. Amo, Phys. Rev. Lett. **112**, 116402 (2014).

[20] M. M. Glazov and L. E. Golub, Phys. Rev. B **77**, 165341 (2008).

[21] M. M. Glazov and L. E. Golub, Phys. Rev. B **82**, 085315 (2010).

[22] E. G. Mishchenko, A. V. Shytov, and B. I. Halperin, Phys. Rev. Lett. **93**, 226602 (2004).

[23] A. A. Burkov and D. G. Hawthorn, Phys. Rev. Lett. **105**, 066802 (2010).

[24] A. A. Burkov, A. S. Núñez, and A. H. MacDonald, Phys. Rev. B **70**, 155308 (2004).

[25] P. Wenk and S. Kettemann, Phys. Rev. B **81**, 125309 (2010).

[26] A. G. Mal'shukov and K. A. Chao, Phys. Rev. B **71**, 121308 (2005).

[27] O. Bleibaum, Phys. Rev. B **72**, 075366 (2005).

[28] O. Bleibaum and S. Wachsmuth, Phys. Rev. B **74**, 195330 (2006).

[29] L. Y. Wang, C. S. Chu, and A. G. Mal'shukov, Phys. Rev. B **78**, 155302 (2008).

[30] X. Liu, X.-J. Liu, and J. Sinova, Phys. Rev. B **84**, 035318 (2011).

[31] H. Flayac, D. D. Solnyshkov, I. A. Shelykh, and G. Malpuech, Phys. Rev. Lett. **110**, 016404 (2013).

[32] H. Terças, D. D. Solnyshkov, and G. Malpuech, Phys. Rev. Lett. **110**, 035303 (2013).

[33] T. A. Fisher, A. M. Afshar, M. S. Skolnick, D. M. Whittaker, and J. S. Roberts, Phys. Rev. B **53**, R10469 (1996).

[34] R. Houdré, C. Weisbuch, R. P. Stanley, U. Oesterle, P. Pellandini, and M. Ilegems, Phys. Rev. Lett. **73**, 2043 (1994).

[35] M. D. Martín, G. Aichmayr, L. Viña, and R. André, Phys. Rev. Lett. **89**, 077402 (2002).

[36] G. Panzarini, L. C. Andreani, A. Armitage, D. Baxter, M. S. Skolnick, V. N. Astratov, J. S. Roberts, A. V. Kavokin, M. R. Vladimirova, and M. A. Kaliteevski, Phys. Rev. B **59**, 5082 (1999).

[37] A. Kavokin, P. G. Lagoudakis, G. Malpuech, and J. J. Baumberg, Phys. Rev. B **67**, 195321 (2003).

[38] K. V. Kavokin, I. A. Shelykh, A. V. Kavokin, G. Malpuech, and P. Bigenwald, Phys. Rev. Lett. **92**, 017401 (2004).

[39] A. Rahimi-Iman, C. Schneider, J. Fischer, S. Holzinger, M. Amthor, S. Höfling, S. Reitzenstein, L. Worschech, M. Kamp, and A. Forchel, Phys. Rev. B **84**, 165325 (2011).

[40] C. Schneider, A. Rahimi-Iman, N. Y. Kim, J. Fischer, I. G. Savenko, M. Amthor, M. Lermer, A. Wolf, L. Worschech, V. D. Kulakovskii *et al.*, Nature (London) **497**, 348 (2013).

[41] P. Wenk, M. Yamamoto, J.-i. Ohe, T. Ohtsuki, B. Kramer, and S. Kettemann, in *Quantum Materials, Lateral Semiconductor Nanostructures, Hybrid Systems, and Nanocrystals* (Springer, 2010), pp. 277–302.

[42] M. Wu, J. Jiang, and M. Weng, Phys. Rep. **493**, 61 (2010).

[43] R. J. Elliott, Phys. Rev. **96**, 266 (1954).

[44] M. I. D'yakonov and V. I. Perel', Sov. Phys. Solid State **13**, 3023 (1972).

[45] Y. Yafet, in *Solid State Physics* (Academic Press, New York, 1963), Vol. 14.
[46] J. Fischer, I. G. Savenko, M. D. Fraser, S. Holzinger, S. Brodbeck, M. Kamp, I. A. Shelykh, C. Schneider, and S. Höfling, Phys. Rev. Lett. **113**, 203902 (2014).
[47] S. Hikami, A. I. Larkin, and Y. Nagaoka, Prog. Theor. Phys. **63**, 707 (1980).
[48] M. Pletyukhov, Phys. Rev. B **75**, 155335 (2007).
[49] P. Kleinert and V. V. Bryksin, Phys. Rev. B **76**, 073314 (2007).
[50] T. L. Hughes, Y. B. Bazaliy, and B. A. Bernevig, Phys. Rev. B **74**, 193316 (2006).
[51] V. E. Sacksteder, S. Kettemann, Q. Wu, X. Dai, and Z. Fang, Phys. Rev. B **85**, 205303 (2012).
[52] S. Pramanik, S. Bandyopadhyay, and M. Cahay, J. Appl. Phys. **104**, 014304 (2008).
[53] A. G. Mal'shukov, K. A. Chao, and M. Willander, Phys. Rev. Lett. **76**, 3794 (1996).
[54] H. Zhao, M. Mower, and G. Vignale, Phys. Rev. B **79**, 115321 (2009).